



HAL
open science

Dynamo tests for stratification below the core-mantle boundary

Peter Olson, Maylis Landeau, Evan Reynolds

► **To cite this version:**

Peter Olson, Maylis Landeau, Evan Reynolds. Dynamo tests for stratification below the core-mantle boundary. *Physics of the Earth and Planetary Interiors*, 2017, 271, pp.1-18. 10.1016/j.pepi.2017.07.003 . hal-03271242

HAL Id: hal-03271242

<https://hal.science/hal-03271242>

Submitted on 25 Jun 2021

HAL is a multi-disciplinary open access archive for the deposit and dissemination of scientific research documents, whether they are published or not. The documents may come from teaching and research institutions in France or abroad, or from public or private research centers.

L'archive ouverte pluridisciplinaire **HAL**, est destinée au dépôt et à la diffusion de documents scientifiques de niveau recherche, publiés ou non, émanant des établissements d'enseignement et de recherche français ou étrangers, des laboratoires publics ou privés.

Dynamo tests for stratification below the core-mantle boundary

Peter Olson^{a,b}, Maylis Landeau^{a,c}, Evan Reynolds^a

^a Department of Earth and Planetary Sciences, Johns Hopkins University, Baltimore MD, USA

^b Department of Earth and Planetary Sciences, University of New Mexico, Albuquerque NM, USA

^c Department of Applied Mathematics and Theoretical Physics, Centre for Mathematical Sciences
Wilberforce Rd., University of Cambridge, Cambridge, UK

July 2, 2017

Abstract

Evidence from seismology, mineral physics, and core dynamics suggests a layer with an overall stable stratification in the Earth's outer core, possibly thermal in origin, extending below the core-mantle boundary (CMB) for several hundred kilometers. Yet vigorous deep mantle convection with locally elevated heat flux implies unstable thermal stratification in some regions below the CMB, consistent with interpretations of non-dipole geomagnetic field behavior that favor upwelling flows in places below the CMB. To resolve this apparent inconsistency, we investigate the structure of convection and magnetic fields in the core using numerical dynamos with laterally heterogeneous boundary heat flux. Strongly heterogeneous boundary heat flux generates localized convection beneath the CMB that coexists with an overall stable stratification there. Our partially stratified dynamos are distinguished by their time average magnetic field structures. Without stratification or with stratification confined to a thin layer, the octupole component is small and the CMB magnetic field structure includes polar intensity minima. With more extensive stratification, the octupole component is large and the magnetic field structure includes intense patches or high intensity lobes in the polar regions. Comparisons with the time-averaged geomagnetic field are generally favorable for partial stratification in a thin (< 400 km) layer but unfavorable for stratification in a thick (~ 1000 km) layer beneath the CMB.

* Corresponding author; e-mail address: olson@jhu.edu (Peter Olson)

Keywords: *Partially stratified dynamos, outer core stratification, core-mantle boundary, core heat flux*

1 Introduction

The possibility of a distinct layer below Earth’s core-mantle boundary (CMB), Braginsky’s (1993) so-called *hidden ocean*, has been the subject of numerous studies using a variety of seismic, geomagnetic, and mineral physics approaches, with the twin objectives of resolving the properties of this layer and understanding its dynamical significance. The majority of these studies conclude that the layer extends one to two hundred kilometers below the CMB (Whaler, 1980; Lay and Young, 1990; Gubbins, 2007; Tanaka, 2007; Buffett, 2014) although some claim it extends to far greater depths, perhaps three hundred kilometers (Helfrich and Kaneshima, 2010; Gomi et al., 2013; Tang et al., 2015) or more (Kaneshima, 2017). Interpretations include stable (subadiabatic) thermal stratification (Gomi et al., 2013; Buffett, 2014) as well as stable compositional stratification due to excess light element concentrations in the layer (Helfrich and Kaneshima, 2013; Gubbins and Davies, 2013).

It is important to point out, however, that not every study supports the existence of such a layer, or at least, there are reasons to doubt that the region below the CMB is uniformly stable to all convective motions. Interpretations of the geomagnetic secular variation are most easily accommodated by core flows including upwelling and downwelling motions that extend to within 100 km below the CMB or shallower (Gubbins, 2007; Amit, 2014; Lesur et al., 2015)). Likewise, the proliferation and rapid evolution of reverse flux spots in the present-day geomagnetic field on the CMB (Olsen et al., 2014) argue for flux expulsion related to upwellings and downwellings (Olson and Amit, 2006).

In addition, it is necessary to consider the effects of the mantle circulation on the geodynamo. Mantle global circulation models (Zhang and Rudolph, 2015; Nakagawa and Tackley, 2013; 2015) predict vigorous deep mantle convection with locally elevated heat flux that is large enough to sustain unstable thermal stratification in some regions beneath the CMB (Olson et al., 2015), even if recent estimates of high thermal conductivity in the core (Ohata et al., 2016) apply. Alternatively, with lower thermal conductivity (Konopkova et al., 2016), thermal conditions may be unstable everywhere, but in that case a small accumulation of light elements at the top of the core (Buffett and Seagle, 2010) could provide the stable stratification.

These issues raise the question of whether it is possible to reconcile seemingly contradictory inferences: a layer providing overall stable stratification on the one hand, with radial

58 motions in the fluid outer core below the CMB on the other. In this paper we address this ap-
59 parent incongruity using numerical dynamos with a particular suite of boundary conditions
60 that (1) model inner core boundary buoyancy release as the source of the main convection,
61 (2) produce an overall (i.e., spherically-averaged) stable thermal stratification below the
62 outer boundary, and (3) generate strong lateral heterogeneity in the stratification, including
63 localized convection. We find that this combination of boundary conditions implies a style
64 of convection in the outer core that dynamically maintains stably stratified conditions in
65 limited regions below the CMB, yet allows for radial motions in places as well as generating
66 a dipole-dominant magnetic field. We call these *partially stratified dynamos*. In addition, we
67 demonstrate that partially stratified dynamos have distinctive high latitude magnetic field
68 structures, allowing the strength of the stratification below the CMB to be inferred remotely,
69 using the geomagnetic field on the CMB.

70 Our study is limited to the types of stratification that are produced when the destabilizing
71 effects of inner core boundary buoyancy release are comparable in the stratified region to the
72 stabilizing effects of subadiabatic CMB heat flux. This regime has been explored previously
73 using numerical dynamos with homogeneous outer boundary conditions (Christensen and
74 Wicht, 2008; Nakagawa, 2011, 2015) and magnetoconvection models (Takehiro and Sasaki,
75 2017). It has been shown that stable stratification tends to filter the non-axisymmetric
76 non-dipolar fields, and if the stratified layer is thick, also reduces the intensity of the axial
77 dipole field (Christensen and Wicht, 2008; Nakagawa, 2011; 2015). Christensen (2016) used
78 combinations of subadiabatic mean boundary heat flux plus lateral boundary variations
79 to produce dynamos with stratification extending below the CMB to 20-40% of the outer
80 core depth. Under these conditions he finds thin horizontal circulations that mediate the
81 boundary heat flux heterogeneity, but little mixing of the stratification. In contrast, stratified
82 magnetoconvection calculations by Takehiro and Sasaki (2017) produce strong flows capable
83 of penetrating most of the stable region.

84 The stratification analyzed in this study refers to radial density gradients that deviate
85 from adiabatic (i.e., uniform entropy) thermal conditions. Temperature gradients resulting
86 from self-compression of the fluid are therefore excluded from our dynamo calculations, and
87 must be factored in before comparing our results to Earth's core. Dynamos that explicitly
88 include adiabatic density and thermal gradients due to compressibility of the fluid also show
89 stratification effects, particularly when the adiabatic density variation is large across the

90 fluid (Jones et al., 2011; Gastine et al., 2012, Yadav et al., 2013). Because the density scale
 91 height of the outer core is greater than its depth, the direct effects of compressibility are not
 92 included in our dynamos. In addition, our study does not consider the situation in which
 93 the stabilizing effects of stratification vastly outweigh the destabilizing effects of inner core
 94 growth, as would be the case for strong, pre-existing compositional stratification (Landeau
 95 et al., 2016) or compositional stratification that develops over time through rapid chemical
 96 diffusion (Nakagawa, 2017). With such strong stratification, lateral variations in heat flux
 97 at the CMB would likely play a more limited role in determining the global structure of the
 98 outer core and its overall dynamical behavior.

99 **2 Partially stratified dynamos**

100 To model dynamo action with thermal and compositional buoyancy originating at the inner
 101 core boundary (ICB) due to inner core growth plus dynamically-regulated thermal stratifi-
 102 cation below the CMB, all within the context of the Boussinesq approximation, we follow
 103 standard procedures (Jones, 2007), defining the codensity C in the outer core as the sum of
 104 densities due to temperature and light element concentration:

$$C = \rho_o (\alpha T + \beta \chi), \quad (1)$$

105 where ρ_o is outer core average density, T is temperature relative to the core adiabat, χ is
 106 the outer core light element concentration relative to its mean, and α and β are volumetric
 107 expansion coefficients for T and χ , respectively. We let $\dot{\chi}_o$ and \dot{T}_o denote the time rate-of-
 108 change of the mean (volume-averaged) light element concentration and temperature of the
 109 outer core, each assumed to be constant over the time span of a single dynamo simulation, so
 110 that $\dot{C}_o = \rho_o (\alpha \dot{T}_o + \beta \dot{\chi}_o)$ is the volume-averaged rate-of-change of codensity over a simulation,
 111 also assumed constant. Further, let Ω denote angular velocity of Earth's rotation, g gravity
 112 at the CMB, $D = r_{cmb} - r_{icb}$ the depth of the outer core fluid, r_{cmb} and r_{icb} being the radii of
 113 the CMB and the ICB, respectively, and let ν and κ denote outer core kinematic viscosity
 114 and codensity diffusivity, respectively.

115 With these definitions, the Boussinesq equations for conservation of momentum including
 116 rotation, conservation of mass, and codensity transport in a rotating spherical shell (see

117 Appendix) include the following dimensionless control parameters:

$$E = \frac{\nu}{\Omega D^2}; \quad Pr = \frac{\nu}{\kappa}; \quad Ra = \frac{\beta g D^5 \dot{\chi}_o}{\nu^2 \kappa}. \quad (2)$$

118 Here E is the Ekman number, Pr is the Prandtl number, and Ra is the Rayleigh number, and
 119 the factors D , D^2/ν and $D^2\rho\beta\dot{\chi}_o/\nu$ scale length, time, and codensity variations, respectively.
 120 Two additional control parameters appearing in the magnetic induction equation and the
 121 codensity equation are the magnetic Prandtl number Pm and the dimensionless volumetric
 122 codensity source/sink ϵ that quantifies the rate of buoyancy absorbed in the outer core from
 123 the mixing of light elements, secular cooling of the outer core, curvature of the core adiabat,
 124 and radioactive heat sources. Our dynamos are driven by the combination of light element
 125 release at r_{icb} and secular cooling, so that

$$\epsilon = -\left(1 + \frac{\alpha \dot{T}_o}{\beta \dot{\chi}_o}\right). \quad (3)$$

126 The magnetic Prandtl number Pm is defined by

$$Pm = \frac{\nu}{\eta} \quad (4)$$

127 where η is the magnetic diffusivity of the outer core. Magnetic fields are scaled by $\sqrt{\rho_o \Omega / \sigma}$,
 128 where σ is electrical conductivity.

129 Additional control parameters arise in defining the boundary conditions. At the ICB we
 130 assume no-slip velocity conditions and a uniform codensity, C_{icb} . At the CMB also assume
 131 no-slip velocity conditions, zero compositional flux, and we specify the heat flux there to be
 132 the sum of a spherical mean part (denoted by an overbar) and a deviation from the spherical
 133 mean (denoted by a prime):

$$q = \bar{q} + q'(\phi, \theta) \quad (5)$$

134 where ϕ and θ are longitude and co-latitude, respectively, and \bar{q} is measured relative to the
 135 heat flux down the core adiabat, with $\bar{q} > 0$ being superadiabatic heat flux and $\bar{q} < 0$ being
 136 subadiabatic heat flux. The variable q' in (5) specifies the pattern and the amplitude of the
 137 CMB heat flux heterogeneity. In the same way we can write the codensity as the sum of a
 138 spherical mean part \bar{C} and a laterally varying part C' . Then using (1) and (5) and assuming
 139 Fourier's law for conduction, the spherical mean and laterally varying codensity gradients
 140 on the CMB can be written as

$$\frac{\partial \bar{C}}{\partial r} = -\left(\frac{\alpha \rho_0}{k}\right) \bar{q} \quad (6)$$

141 and

$$\frac{\partial C'}{\partial r} = - \left(\frac{\alpha \rho_0}{k} \right) q' \quad (7)$$

142 where r is the radial coordinate and k is the thermal conductivity of the outer core, assumed
 143 constant. In dimensionless form (6) and (7) become

$$\frac{\partial \bar{C}^*}{\partial r^*} = \frac{Ra_{\bar{q}}}{Ra} = S, \quad (8)$$

144 where

$$S = - \left(\frac{\alpha \nu}{D k \dot{\chi}_o} \right) \bar{q} \quad (9)$$

145 is the dimensionless stratification parameter we use in this study, and

$$\frac{\partial C'^*}{\partial r^*} = \frac{Ra_{q'}}{Ra} L(\theta, \phi) = S' L. \quad (10)$$

146 In (8)

$$Ra_{\bar{q}} = - \left(\frac{\alpha g D^4}{k \nu \kappa} \right) \bar{q} \quad (11)$$

147 is the Rayleigh number based on the spherical mean CMB heat flux, and in (10)

$$Ra_{q'} = \frac{\alpha g D^4}{k \nu \kappa} \Delta q' \quad (12)$$

148 is the Rayleigh number based on the peak-to-peak variation $\Delta q'$ of the laterally varying
 149 CMB heat flux, $L(\theta, \phi)$ being the pattern (or planform) of its lateral variation in terms of
 150 colatitude θ and longitude ϕ , S' is the boundary heterogeneity counterpart to S , and the
 151 asterisks denote dimensionless variables. Note that both S and $Ra_{\bar{q}}$ are defined to be positive
 152 when \bar{q} is negative, i.e., when the mean CMB heat flux is stabilizing.

153 In this study we restrict consideration to dynamos with $Pr = 1$, $Pm = 6$, and $\epsilon =$
 154 -0.8 , the latter appropriate for dominantly compositional convection but with some secular
 155 cooling. In most cases we choose Ekman numbers $E = 1 \times 10^{-4}$, with a few cases at
 156 $E = 3 \times 10^{-5}$. We fix the aspect ratio of the fluid outer core to be $r_{icb}/r_{cmb} = 0.351$.
 157 The solid region $r \leq r_{icb}$ representing the inner core is assumed to have the same electrical
 158 conductivity σ as the fluid, and the solid region $r \geq r_{cmb}$ representing the mantle is assumed
 159 to be electrically insulating.

160 By fixing the codensity on the inner boundary, we allow the codensity flux there to freely
 161 adjust, which permits it to respond to the heterogeneous CMB heat flux in a dynamically
 162 consistent way. For modeling convective interaction between the inner core and the mantle,

163 this boundary condition has advantages over other simplified boundary conditions, such as
 164 fixing the ICB codensity flux *a-priori*, because it naturally yields lateral variations in the
 165 ICB codensity flux, which is a dynamo model proxy for lateral variations in the rate of
 166 inner core growth. Its main disadvantage in the context of our study is that it requires two
 167 global Rayleigh numbers with different definitions to characterize these dynamos: $Ra_{\bar{q}}$ for
 168 the CMB forcing that depends inversely on viscosity and Ra for the ICB forcing that depends
 169 inversely on viscosity squared. Their ratio, the stratification parameter S , therefore depends
 170 linearly on the fluid viscosity, which unfortunately is poorly constrained in the outer core.
 171 Similarly, by setting the sink function ϵ to a constant we let the dynamics determine the
 172 thickness and the gravitational stability of the stratified region, through interactions between
 173 the control parameters Ra , S , S' . An alternative approach is to prescribe the thickness of
 174 the stratification by tuning the sink function, as in Nakagawa (2015). Later we show that
 175 these two approaches yield broadly consistent results in terms of the time average dynamo
 176 magnetic field structure.

177 We examine dynamo action over ranges of the control parameters Ra and S , for three
 178 different CMB heat flux planforms L . The first planform, denoted by $L0$, corresponds to
 179 uniform CMB heat flux, with $C'^* = 0$ everywhere on the outer boundary. These uniform
 180 boundary cases serve as references for the heterogeneous boundary cases. The second plan-
 181 form, denoted by $L2$, is defined by C'^* on the outer boundary consisting of spherical harmonic
 182 degree two components, and is shown in Figure 1a. The third planform, denoted by $L4$, con-
 183 sists of C'^* components up to and including spherical harmonic degree four, is shown in
 184 Figure 1b.

185 The $L4$ planform in Figure 1b was obtained from the present-day CMB heat flux pat-
 186 tern produced by the mantle GCM (mantle global circulation model) HF5 of Rudolph and
 187 Zhong (2014) and Zhong and Rudolph (2015), after truncating that CMB heat flux pattern
 188 at spherical harmonic degree and order four. The mantle GCM HF5 includes variable man-
 189 tle viscosity, compositionally dense material at the mantle base, plus plate motion surface
 190 velocity constraints starting around 400 Ma and continuing to present-day. This particular
 191 mantle GCM has been used by Olson et al. (2015) to model core evolution. The mean and
 192 standard deviation of its present-day CMB heat flux are 79 ± 24 mW/m², and its maximum
 193 and minimum are 131 and 36 mW/m², respectively. The $L2$ planform in Figure 1a is a mod-
 194 ified version of $L4$ planform using only spherical harmonic degree $\ell=2$ components at orders

195 $m=0$ and $m=2$, adjusted to create a pattern with bilateral (i.e., 2-fold) azimuthal symmetry.
 196 The $L2$ pattern in Figure 1a corresponds to the largest scale, lower mantle heterogeneity
 197 structure advocated by some seismologists (Dziewonski et al., 2010). It has the same mean
 198 value as the $L4$ pattern, whereas its extreme values are 137 and 31 mW/m², respectively. It
 199 is essentially the same planform used by Olson and Amit (2015) in their study of the effects
 200 of dense basal mantle piles on magnetic polarity reversal behavior.

201 The stratification parameter S in our dynamos are determined according to (8) and (9).
 202 The amplitudes of the boundary heterogeneity S' of the $L2$ and $L4$ patterns in our dynamos
 203 are scaled using the following ratio:

$$\Gamma = |S'L| \left(\frac{\partial \bar{C}^*}{\partial r_{icb}^*} \right)^{-1}, \quad (13)$$

204 where $||$ denotes peak-to-peak variation. The Γ ratio can be estimated by combining the
 205 results of our mantle GCM with a model of the thermodynamic state of the core. We use a
 206 core state model with the CMB heat flux obtained from the mantle GCM (which includes an
 207 adiabatic part, assumed to be 96 mW/m²) to estimate the implied CMB and ICB codensity
 208 fluxes and hence the ratio Γ . We find that the mean cmb heat flux from mantle GCMs with
 209 plate motion constraints (Zhong and Rudolph, 2015) is typically comparable to the adiabatic
 210 core heat flux, such that $\Gamma \simeq (r_{icb}/r_{cmb})^2 \simeq 0.123$, approximately. We calculate the spherical
 211 mean ICB codensity flux from our numerical dynamo at a given Ra with $Ra_{\bar{q}} = Ra_{q'}=0$,
 212 and then adjust $|S'L|$ in (13) so that $\Gamma=0.123$ for that dynamo. The above steps yield a
 213 constant value of $|S'L|=0.58$ for all the $L2$ dynamo cases. A similar procedure is followed
 214 for the $L4$ dynamo cases. Amplitude coefficients of the spherical harmonics that generate
 215 these $L2$ and $L4$ heat flux planforms for our dynamos are given in Table A1.

216 We have carried out a systematic parameter sweep of stratified thermochemical convec-
 217 tion and dynamo action with the control parameters just described, using the MAGIC code
 218 (Wicht, 2002), varying the parameters Ra and S for the three outer boundary heat flux
 219 heterogeneity patterns $L0$, $L2$ and $L4$. Table A2 summarizes the control parameter ranges
 220 of our sweep. Most of the calculations were done at $E = 1 \times 10^{-4}$ and run for at least 5
 221 viscous diffusion times in order that the run averages approximate true time averages. For
 222 these calculations we used a numerical grid with $(n_r, n_\theta, n_\phi) = (81, 128, 256)$ in the fluid
 223 shell and spherical harmonic truncation $(\ell, m)_{max}=85$. We also ran one case at $Ra = 2 \times 10^7$
 224 with $S=1.0$, which was strongly subcritical for convection. The majority of our calculations

225 used the $L2$ boundary heterogeneity, although uniform $L0$ as well as some $L4$ cases were
 226 included for comparison purposes. Overall, we found that the $L4$ cases mostly added shorter
 227 wavelength heterogeneity to the $L2$ case results, somewhat complicating their interpretation
 228 without changing their behavior in a fundamental way. We also computed three $S = 0.1$
 229 cases at $E = 3 \times 10^{-5}$ with $L0$, $L2$, and $L4$ boundary heterogeneity, respectively, which are
 230 given in in Table A2. For the smaller E calculations we used a numerical grid with (n_r, n_θ, n_ϕ)
 231 $= (121, 192, 384)$ in the fluid shell and spherical harmonic truncation $(\ell, m)_{max}=128$.

232 **3 Dynamo results**

233 Figure 2 shows $E = 1 \times 10^{-4}$ cases in terms of the control parameters we varied. Axes are
 234 the Rayleigh number Ra and the stratification parameter S , defined as positive for stable
 235 boundary stratification and negative for unstable boundary stratification. The dashed line
 236 marks neutral (i.e., adiabatic) boundary flux cases. $L0$ (squares), $L2$ (crosses) and $L4$ (cir-
 237 cles) denote spherical harmonic representation of the outer boundary heat flux heterogeneity
 238 as described in the previous section.

239 The combined effects on the fluid motions of stable stratification and lateral boundary
 240 heterogeneity can be seen by comparing Figures 3 and 4, which show equatorial plane and
 241 global surface views of the time average flow structure at $E = 1 \times 10^{-4}$ and $Ra = 2 \times 10^7$, with
 242 $L0$ (uniform) and $L2$ boundary heterogeneity, respectively, for two stratification parameters.
 243 With a uniform outer boundary, the time average codensity is spherically symmetric for both
 244 stabilizing (Figure 3a, b, c) and destabilizing (Figure 3d, e, f) stratification parameter. The
 245 only difference between the two cases is the presence of stable stratification in the $S=0.2$
 246 case, extending downward from the outer boundary for a distance equal to about one quarter
 247 of the fluid shell depth. This stable stratification has major influences on the fluid velocities,
 248 as can be seen in the radial (u_r) and azimuthal (u_ϕ) images in Figure 3. In both cases the
 249 radial velocities are highest near the inner boundary, where the buoyancy release is greatest,
 250 but in the $S=0.2$ case the radial velocities are truncated at the depth where stratification
 251 begins, and fail to penetrate to the outer boundary. Comparable differences are seen in the
 252 azimuthal velocity near the outer boundary, where in the $S=-0.1$ case the highest velocities
 253 occur at high latitudes, within and near the inner core tangent cylinder, whereas in the
 254 $S=0.2$ case the highest velocities occur in a retrograde (westward flowing) equatorial jet.

255 Figure 4 has the same control parameters as Figure 3 but with $L2$ boundary heterogene-
 256 ity added. In the destabilizing $S=-0.1$ case the stratification is highly destabilizing below
 257 the regions of higher than average boundary heat flux, and beneath these regions the time
 258 average radial velocity is strongly negative (downward flow). Conversely, below the regions
 259 of lower than average boundary heat flux the stratification is weakly stable and the time
 260 average radial velocity is positive (upward flow), from the inner boundary all the way to
 261 the outer. In contrast, in the $S=0.2$ case the thermal stratification is stabilizing at all lon-
 262 gitudes immediately below the outer boundary and the radial velocity pattern is layered.
 263 Downwellings located below high boundary heat flux regions penetrate only about one quar-
 264 ter of the fluid depth before terminating, and the laterally broad upwellings below regions
 265 with low outer boundary heat flux show layering, with the strongest upwelling layers occur-
 266 ring immediately below the outer boundary and also just above the inner boundary. The
 267 azimuthal velocity patterns beneath the outer boundary for both $S=-0.1$ and $S=0.2$ cases
 268 include, at low latitudes, thin lenses of eastward (prograde) flow immediately beneath the
 269 high boundary heat flux regions but displaced slightly in the downstream direction of the
 270 heterogeneity, plus generally westward (retrograde) flow beneath the low boundary heat flux
 271 regions, again displaced slightly downstream of the center of the boundary heterogeneity.

272 The other major difference between cases with versus without stabilizing boundary heat
 273 flux, which we later show is crucial for stratification detection, is the pattern and strength of
 274 the circulation inside the tangent cylinder of the inner boundary. The cases with destabilizing
 275 outer boundary fluxes in both Figures 3 and 4 have stronger azimuthal flows inside the
 276 tangent cylinder compared to their counterparts with stabilizing outer boundary fluxes.
 277 This difference indicates that the pattern of convection at depth inside the tangent cylinder
 278 is different with versus without boundary stabilization, and as we demonstrate next, this
 279 has observable effects on the magnetic fields generated in the tangent cylinder region.

280 Figure 5 shows global views of the time average dynamo structure on and just below the
 281 outer boundary and in cross section, at $E = 1 \times 10^{-4}$ and $Ra = 6 \times 10^7$, for stratification
 282 parameters $S= 0$ (neutral), $S=0.2$, and $S=0.3$, respectively, all with $L2$ boundary hetero-
 283 geneity. The radial magnetic field on the outer boundary in the neutral case Figure 5a has
 284 higher intensity and shorter length scales in its structure, compared to its counterparts with
 285 stabilizing boundary heat flux, because without stratification, the short length scale fluctu-
 286 ations are more intense and require longer run times to average out. More importantly, the

287 high latitude structure of the neutral $S = 0$ dynamo includes rings of high intensity radial
288 magnetic field localized near the latitudes that correspond to the inner boundary (inner core)
289 tangent cylinder in each hemisphere, plus conspicuous polar intensity minima in both north
290 and south hemispheres. In contrast, the high latitude radial magnetic field in the $S = 0.2$
291 dynamo consists of patches of high intensity field that terminate short of the pole and no
292 polar intensity minima, while the high latitude radial magnetic field in the $S = 0.3$ dynamo
293 consists of lobes of high intensity field that extend all the way to the poles, forming polar
294 intensity maxima.

295 The differences in these field structures can be directly attributed to differences in the
296 high latitude pattern of radial velocity in the two cases. As seen in Figure 5b, there are
297 strong polar upwellings in the $S = 0$ case, whereas Figure 5e shows much weaker polar
298 upwellings in the $S=0.2$ case, and Figure 5h shows polar downwellings in the more strongly
299 stabilized $S = 0.3$ case. Accordingly, the magnetic field becomes concentrated near the pole
300 in the most stratified case, the two high intensity flux lobes being located along longitudes
301 that approximately correspond to the bands of radial downward flow, whereas in the neutral
302 $S=0$ case the field is mostly concentrated by the circular downwellings that occur along the
303 tangent cylinder. The intermediate $S=0.2$ case produces a field structure that results from
304 a mixture of the flows seen in the two more extreme cases.

305 Patterns of the azimuthally and time averaged internal structure are shown in Figures
306 5c, f, and i for each of the three dynamos. These images reveal the underlying dynamics
307 that produce distinct radial velocity structures, which in turn produce the polar magnetic
308 intensity minima, patch, or lobe radial magnetic field structures. In the $S=0$ case the
309 tangent cylinder region is supercritical for convection and has the familiar combination of
310 polar upwellings plus tangent cylinder downwellings in its azimuthal averaged flow structure
311 (Olson and Aurnou, 1999; Sreenivasan and Jones, 2005). Together these up- and down-
312 flows create a circulation that tends to expel poloidal magnetic field from inside the tangent
313 cylinder region. In contrast, in the strongly stabilized $S=0.3$ case the tangent cylinder is
314 (or appears to be) subcritical for free convection and the flow directions are reversed there
315 relative to the $S=0$ case. Magnetic flux concentration, rather than flux expulsion, is active
316 inside the tangent cylinder in this case. In the intermediate $S=0.2$ case there is a weak
317 polar upwelling, slightly concentrating the field inside the tangent cylinder. Consequently,
318 the radial field becomes more concentrated in the polar regions with stronger stratification,

319 eliminating the polar intensity minimum and replacing it with high intensity field that, with
 320 the $L2$ boundary heterogeneity, generates high intensity patches or lobes. The high intensity
 321 flux lobes or patches are located approximately at the longitudes that correspond to the
 322 bands of radial downward flow (Figures 5e and h). We note that the dynamics of the flows
 323 that underlie the structural changes in the field here are similar to what has been found
 324 in dynamos when the ratio of inner boundary-to-outer boundary radius is changed, as is
 325 expected to be the situation before versus after the inner core nucleates (Landeau et al.,
 326 2017).

327 As with the magnetic field structure, major differences in the structure of the internal
 328 azimuthal flows in Figures 5c, f, and i lie at polar latitudes, where the neutral $S=0$ case
 329 includes a strong retrograde (westward) polar vortex that extends to the outer boundary,
 330 whereas in the $S=0.3$ case the flow in the same region is strongly attenuated in amplitude
 331 and weakly prograde (eastward). Equatorial westward jets are present in all three cases, but
 332 they are stronger with stratification, and unlike the polar flows, penetrate to near the outer
 333 boundary, even in the most stabilized $S=0.3$ case. Qualitatively, this behavior is in accord
 334 with previous findings by Nakagawa (2011) and Takehiro and Sasaki (2017).

335 In order to systematize how these morphologic differences in the magnetic field struc-
 336 ture vary with our dynamo control parameters, we show in Figure 6 a regime diagram of
 337 the magnetic field in the polar region for the $E = 1 \times 10^{-4}$ and $L2$ boundary heterogene-
 338 ity cases. Axes are Rayleigh number Ra and outer boundary stratification parameter S ,
 339 once again positive for stable stratification, negative for unstable. Other symbols denote
 340 the structure of the time average radial magnetic field structure on the outer (core-mantle)
 341 boundary at high latitudes. M denotes existence of polar intensity minima, P denotes high
 342 field intensity patches without polar minima, L denotes high field intensity lobes without
 343 polar minima, and N (no dynamo) denotes subcritical for dynamo action due to excessively
 344 strong boundary-induced stratification. Dual symbols in Figure 6 denote high latitude mag-
 345 netic field structures that appear to be transitional, M/P for polar minima transitioning to
 346 patches, and P/M for the reverse. This figure demonstrates there are several (3 or more) dis-
 347 tinctive magnetic field structures that occur systematically as the control parameters vary,
 348 and that these structures are particularly sensitive to the stratification parameter S , al-
 349 though some weaker dependence on the Rayleigh number Ra is evident from the locations of
 350 the transitional cases. In particular, the patches P-regime appears to attenuate and possibly

351 disappear at strongly supercritical Rayleigh numbers. With more modest supercriticality,
 352 the sequence with increasing S consists of M for unstable, neutral, or very weakly stratified
 353 cases, transitioning to P with slightly stronger stratification, then to L and finally to N when
 354 the boundary-induced stratification is strong enough to kill dynamo action. With reference
 355 to Table A2, our three $S = 0.1$ cases at $E = 3 \times 10^{-5}$ and $Ra = 2 \times 10^8$ are all in the
 356 M-regime, consistent with the results shown in Figure 6.

357 The distinctions between M, P, and L field structures involves arbitrary considerations
 358 in some of the transitional cases, but in most situations, identification can be made on
 359 the basis of contours of B_r on the dynamo outer boundary in the polar regions. Figure 7
 360 shows contours of the time-averaged radial magnetic field intensity on the outer boundary
 361 for the three dynamos shown in Figure 5. Black curves are contours that enclose the high
 362 field intensity regions in each case. If two contours are needed to enclose the B_r -intensity
 363 maxima and both contours include the pole, the structure is classified as M-type, as in Figure
 364 7a. Note that the two bounding contours should not be very different in radius, so as to
 365 exclude from consideration very small, inconsequential field intensity minima. Alternatively,
 366 if two bounding contours are needed and neither contour includes the pole, the structure
 367 is classified as P-type, as in Figure 7b. Finally, if a single bounding contour encloses the
 368 intense field and also includes the pole, the structure is classified as L-type, as in Figure 7c.

369 The three magnetic field structures in Figure 7 are distinct because of the combined ac-
 370 tion of the stratification measured by S or alternatively $Ra_{\bar{q}}$, plus the $L2$ lateral boundary
 371 heterogeneity measured by S' or alternatively $Ra_{q'}$. Other parameter combinations could
 372 lead to different results. For example, eliminating the lateral boundary heterogeneity yields
 373 axisymmetric time averaged magnetic structures, so that the M- and L-structures trans-
 374 form to axisymmetric polar minima and axisymmetric polar maxima, respectively, while the
 375 regime with clearly defined P-structures probably gets lost. The radial magnetic field struc-
 376 tures in figures 3 and 5 of Nakagawa (2015), calculated using homogeneous outer boundary
 377 conditions in the same range of Ekman and magnetic Prandtl numbers, support this inter-
 378 pretation. This behavior, along with the inference from Figure 6 that the P-regime becomes
 379 attenuated at highly supercritical Ra suggests that the high intensity patch regime may be
 380 less robust than polar intensity minima or maxima. In addition, reducing the symmetry of
 381 the boundary heterogeneity can produce different results, by obscuring the clear-cut differ-
 382 ences in the high latitude structures found with $L2$ symmetry. For example, we find that

383 the loss of bilateral symmetry with $L4$ boundary heterogeneity yields a nominally P-style
 384 field morphology, but with a single rather than two high field intensity patches. However, in
 385 spite of these complications, our results suggest it is possible to probe Earth’s outer core for
 386 stratification using time average geomagnetic field morphology in the polar regions.

387 Figure 8 shows additional stratification diagnostics that involve ratios $G\ell 0$ of the axial
 388 ($m=0$) Gauss coefficients of the magnetic field, obtained by time-averaging our partially
 389 stratified dynamos. Figure 8a shows axially symmetric ($m=0$) Gauss coefficient ratios $G\ell 0 =$
 390 $g(\ell, 0)/g(1, 0)$ versus spherical harmonic degree ℓ from time-averaged dynamos with $Ra =$
 391 6×10^7 and $L2$ boundary heterogeneity, for various stratifications S . Figure 8b shows Gauss
 392 coefficient ratio $G30$ (axial octupole over axial dipole) versus stratification S for the same
 393 dynamos. M,P,L denote polar minima, patches, and lobes, respectively, in the high latitude
 394 magnetic field structure. Stable/unstable refers to the sign of the gravitational stability
 395 below the outer boundary. In Figure 8a the only appreciable (i.e., observable) G-ratio is
 396 $G30$. The $G50$ ratios change sign with stratification but are too small to be observed. In
 397 Figure 8b, $G30$ is positive for all S -values considered, although it might become negative
 398 for very strongly unstable stratification. More significantly, $G30$ increases with S , perhaps
 399 saturating around 0.15 near $S=0.2$.

400 4 Stratification scaling

401 Before applying our results to thermal stratification in Earth’s outer core, a necessary first
 402 step is to derive scaling laws that summarize the strength and extent of the stratification in
 403 our numerical dynamos as a function of the control parameters. The two control parameters
 404 that we varied substantially are the Rayleigh number Ra and the stratification parameter
 405 S , or alternatively, the boundary Rayleigh number $Ra_{\bar{q}}$. Furthermore, most of our dynamos
 406 used the $L2$ boundary heat flux heterogeneity with the other control parameters fixed (that
 407 is, $E = 1 \times 10^{-4}$, $Pr = 1$, $Pm = 6$). Accordingly, our fits are biased toward dynamos of this
 408 type. In addition, we focus attention on two parameterizations of the stratification: (1) the
 409 spherically averaged thickness of the stratified region beneath the outer boundary and (2)
 410 the spherically averaged gravitational stability of the layer, both given in Table A2 for each
 411 case.

412 We define the spherically averaged dimensionless thickness of the stratified region to be

$$\delta^* = \frac{r_{cmb} - r_{min}}{r_{cmb}} \quad (14)$$

413 where r_{cmb} is, as before, the outer boundary radius and r_{min} is the radius where \bar{C}^* reaches
 414 its local minimum value below the outer boundary, \bar{C}_{min}^* , as seen in Figure 3d. Similarly,
 415 we define the characteristic gravitational stability of this region in terms of the following
 416 parameter:

$$N^{*2} = \frac{\delta C^*}{\delta^*}, \quad (15)$$

417 where $\delta C^* = \bar{C}_{cmb}^* - \bar{C}_{min}^*$ is the dimensionless codensity increase across the stratified
 418 region. The choice of the notation here is motivated by the connection between N^* and the
 419 buoyancy frequency in stratified fluids (Turner, 1980), the asterisk emphasizing that this is
 420 a nondimensional parameter.

421 Figure 9 shows fits of the dimensionless stratified layer thickness to power laws in Ra ,
 422 $Ra_{\bar{q}}$, and S . In Figure 9a we assume a power law of the form

$$\delta^* = a Ra_{\bar{q}}^b Ra^c \quad (16)$$

423 where a is a (constant) coefficient and b and c are (constant) exponents. The fit was obtained
 424 by minimizing the function

$$F = \sum \frac{\delta^{*2}}{\sigma_{\delta}^2} (\log \delta^* - \log a - b \log Ra_{\bar{q}} - c \log Ra)^2, \quad (17)$$

425 where σ_{δ} , the characteristic uncertainty on δ^* , was assumed to be the same for all cases. The
 426 symbols in Figure 9a have the same meaning as in Figure 2 and the color scheme indicates
 427 the different magnetic field structures. Cases with $\delta^*=0.6491$ are saturated, meaning that
 428 the stratification spans the entire fluid layer from r_{cmb} to r_{icb} . Excluding saturated cases
 429 yields $(a, b, c)=(1.26, 1.2, -1.18)$ for the best-fitting constants in (16).

430 Figure 9a reveals that the thickness of the stratified region increases strongly with $Ra_{\bar{q}}$ and
 431 decreases about equally strongly with Ra , as anticipated on physical grounds. Significantly,
 432 the exponents in Figure 9a nearly satisfy the relationship $c = -b$, which implies that the
 433 thickness of the stratified layer is solely a function of the stratification parameter S . We
 434 explain the latter result by considering mass conservation in the stratified layer : assuming
 435 zero mass anomaly flux at the base of the stratified layer (i.e. zero codensity gradient),
 436 one obtains from mass balance that the volume of the layer evolves as $-Ra_{\bar{q}}/(Ra\epsilon) =$

437 $-S/\epsilon$, implying that the stratified layer volume depends solely on S for constant volumetric
 438 codensity source/sink ϵ . Accordingly, (16) reduces to

$$\delta^* = aRa_{\bar{q}}^bRa^{-b} = a_{\delta}S^b, \quad (18)$$

439 assuming $c = -b$. Figure 9b shows the best fit to (18) found by minimizing (17) with S in
 440 place of $Ra_{\bar{q}}^bRa^c$. The best-fitting coefficient and exponent become $(a_{\delta}, b) = (1.82, 1.2)$.

441 The only systematic discrepancies between stratified layer thickness and our scaling occur
 442 at low S values, for cases with heterogeneous heat flux. This can be explained as follows.
 443 The lateral heat flux variations produce a mix of regions that are convectively unstable below
 444 the outer boundary and regions that are convectively stable. Because the thermal boundary
 445 layer in convecting regions is thinner than the stratified layer in stable regions, the volume-
 446 averaged codensity field is biased toward the properties of the stable region. Accordingly,
 447 the globally averaged stratified thickness is non-zero with strong heterogeneous boundary
 448 conditions, even in cases with $S=0$.

449 The gravitational stability immediately below the CMB is measured by the squared
 450 buoyancy frequency defined in terms of CMB heat fluxes:

$$N_{cmb}^2 = \frac{\alpha g}{k}(q_{ad} - \bar{q}_{total}), \quad (19)$$

451 where q_{ad} and \bar{q}_{total} refer to the adiabatic and mean CMB heat fluxes, the latter including the
 452 adiabatic contribution. The property values in Table A3 yield $N_{cmb}^2 = 2.4 \times 10^{-8}$ (rad/s)², so
 453 that the ratio of the squared buoyancy frequency to the square of the Coriolis parameter is
 454 approximately $(N_{cmb}/2\Omega)^2 \simeq 1.1$. However, this measure of the gravitational stability applies
 455 only in a very limited depth range beneath the CMB, essentially within a thin boundary
 456 layer region where the codensity gradient is conductive. In particular, it does not apply over
 457 the entire depth range of the stratification, because the codensity gradient there is affected
 458 by convection.

459 A better measure of the overall gravitational stability is the average of the buoyancy
 460 frequency over the stratified region, given by (15). Figure 10 shows the dependence of
 461 N^{*2} defined by (15) on Ra , $Ra_{\bar{q}}$, and S for all cases with $S < 0.4$. The symbols and color
 462 scheme are the same as in Figure 9. Figure 10a shows that the best-fitting constants in a
 463 power-law relationship with Ra and $Ra_{\bar{q}}$ similar to (16) are $(a, b, c) = (1.1, 1.05, -1.07)$. Within
 464 uncertainties, the condition $c = -b$ again holds in this case, indicating that the gravitational

465 stability also depends primarily on S . The latter result implies that the mean stratification
 466 across the layer is proportional to the stabilizing codensity gradient imposed at the CMB .
 467 Refitting the stability data to

$$N^{*2} = a_N S^b \quad (20)$$

468 with $b = 1$ yields $a_N = 0.72$, the fit shown by the dashed line in Figure 10b. The deviations
 469 from linear scaling at $S \geq 0.4$ result from weak or non-existent convection from the inner
 470 core buoyancy source.

471 5 Extrapolation to the outer core

472 Table A3 gives values of the physical properties needed to calculate the stratification param-
 473 eter in the outer core according to the definition of S in (9). We use the core state model
 474 described in Olson et al. (2015) with the adiabatic thermal gradient as modified by Labrosse
 475 (2015), which for a thermal conductivity $k=100$ W/m/K gives and adiabatic heat flux at the
 476 CMB of $q_{ad} = 96$ mW/m². We select $\bar{q}_{total} = 79$ mW/m², representative of the mean CMB
 477 heat flux from mantle GCMs (Nakagawa and Tackley, 2015; Zhong and Rudolph, 2015),
 478 which includes the adiabatic conductive contribution. Together these imply a subadiabatic
 479 heat flux at the CMB, with $\bar{q} = \bar{q}_{total} - q_{ad} = -17$ mW/m². The core state model then yields
 480 $\dot{C}_o = 6.8 \times 10^{-16}$ kg/s for the rate of codensity change in the outer core due to the combined
 481 effects of cooling and light element increase.

482 Substituting \dot{C}_o , \bar{q} , and the other parameter values from Table A3 into (9) yields a low
 483 value of $S=0.018$ for an outer core viscosity of $\nu = 2 \times 10^{-6}$ m²/s, an intermediate value of
 484 $S=0.064$ for $\nu = 3.5 \times 10^{-6}$ m²/s and a high value of $S=0.2$ for an outer core viscosity of
 485 $\nu = 2.2 \times 10^{-5}$ m²/s. Here we have adjusted the diffusivity so that $\kappa = 10\nu$ in all cases.
 486 Application of our scaling law (18) with $a_\delta=1.82$ and $b=1.2$ yields stratified layer thickness
 487 predictions of $\delta = 52$ km, 230 km, and 920 km, respectively, for these three viscosity choices.
 488 The stratified layer thickness also depends sensitively on \bar{q}_{total} . For example, reducing \bar{q}_{total}
 489 to 50 mW/m² and assuming an outer core kinematic viscosity of $\nu = 2 \times 10^{-6}$ or $\nu = 7 \times 10^{-6}$
 490 m²/s along with the other properties in Table A3, the predicted stratified layer thickness
 491 would be 255 km or 1150 km, respectively.

492 The dependence of stratified layer thickness on viscosity in our scaling is a consequence
 493 of the definition of S , which is the ratio of two Rayleigh numbers, one based on the outer

494 boundary codensity flux, the other based on the rate of codensity change in the outer core as a
 495 whole. It could be argued that Ohmic rather than viscous dissipation should control the layer
 496 thickness in the Earth’s core, and the dependence of layer thickness on viscosity is therefore
 497 a model artifact. Nevertheless, the above range encompasses most previous estimates of the
 498 thickness of the outer core stratified region, and as we demonstrate below, the gravitational
 499 stability of the stratified layer predicted by our scaling is nearly independent of viscosity.

500 To apply our scalings to the gravitational stability of a stratified layer in the outer core,
 501 we combine (9) and (20) to get, in terms of dimensional properties,

$$N_{ave}^2 = a_N \frac{\alpha g}{k} (q_{ad} - \bar{q}_{total}). \quad (21)$$

502 The property values listed in Table A3 give $N_{ave}^2 = 1.7 \times 10^{-8} \text{ (rad/s)}^2$. Note that the layer
 503 average gravitational stability (21) is reduced from its value immediately below the CMB
 504 (20) by the factor $a_N=0.72$, but otherwise its dependence on the properties of the outer
 505 core remains the same. Also, (21) implies that, unlike the thickness of the stratified layer,
 506 the gravitational stability does not depend explicitly on the inner core buoyancy source or
 507 the outer core viscosity. This is a consequence of our ignoring the (very weak) dependence
 508 of N^{*2} on Ra in Figure 10. Finally, there appears to little dependence of the stratification
 509 parameters on the Ekman number, especially the buoyancy frequency. For example, $N^{*2} =$
 510 0.0649 for the $L2, S = 0.1 E = 3 \times 10^{-5}$ case in Table A2, compared to an average value of
 511 $N^{*2} = 0.0678$ all of the $L2 S = 0.1$ cases at $E = 1 \times 10^{-4}$, just a 4% change in gravitational
 512 stability accompanying three-fold change in rotation rate.

513 6 Testing for outer core stratification

514 Our results show that the combination of subadiabatic average heat flux plus large amplitude
 515 lateral variations in heat flux generates an overall stable stratification below the CMB, yet
 516 allows for localized radial motions where the CMB heat flux is particularly large. This partial
 517 stratification contrasts with the usual assumption of homogeneously stratified conditions, in
 518 which radial motions would be suppressed uniformly.

519 Our partially stratified dynamos show clearly identifiable transitions in the structure
 520 of the time-averaged radial magnetic field in polar regions that correspond to increasing
 521 strength of stable stratification, starting from polar minima without stratification (or with

522 weak stratification), to patches of intense field for moderate stratification, finally to lobes of
523 intense field for stronger stratification. Dynamos with homogeneous outer boundaries lack
524 permanent patch or lobe structures, and switch from polar minima to polar maxima with
525 increasing stratification (Nakagawa, 2015).

526 The structural transitions we find with heterogeneous outer boundary conditions offer
527 the possibility of inferring the stratification below the CMB based on the morphology of the
528 time-averaged geomagnetic field on the CMB. In order to realize this possibility, however, it
529 is necessary to image the high latitude geomagnetic field with sufficient resolution and over
530 a sufficiently long period of time, in order to image its nonaxisymmetric structure. It is not
531 obvious that current models of the time average geomagnetic field satisfy these requirements.

532 The present-day geomagnetic field on the CMB has been imaged up to a maximum spher-
533 ical harmonic degree of approximately $\ell_{max}=14$, as shown in Figure 12a. At this resolution,
534 polar minima are clearly evident, and there is even reversed magnetic flux in the polar regions
535 of both hemispheres. The northern hemisphere structure has previously been interpreted as
536 evidence of a convective upwelling associated with a polar vortex (Olson and Aurnou, 1999).
537 When the geomagnetic field is time-averaged over the past 400 yr, as in field model `gufn1` by
538 Jackson et al. (2000), both polar minima are strongly attenuated compared to the present-
539 day, and the time-averaged field structure is more patch-like at high latitudes. This trend
540 continues in field reconstructions with increasingly long time averages. In archeomagnetic
541 field reconstructions such as CALS10k (Korte et al., 2011), time averaging over thousands of
542 years results in high latitude field structures that are distinctly more lobe-like, compared to
543 the present-day, with no expression of polar minima. Finally, paleomagnetic field reconstruc-
544 tions that average the geomagnetic field over the past five million years (0-5Ma) typically
545 only show broad, reduced intensity lobe structures in the polar regions (Johnson and Consta-
546 ble, 1995). But even these modest deviations from axial symmetry have been questioned, as
547 it remains unclear that the paleomagnetic data absolutely requires their existence (Johnson
548 and McFadden, 2015).

549 Superficially, the tendency for geomagnetic and paleomagnetic field reconstructions to
550 exhibit broad, high latitude lobes with increasingly long time averaging would implicate
551 moderate or strong stratification beneath the CMB, characterized by a stratification pa-
552 rameter $S > 0.2$, according to our results. However, there is an alternative interpretation.
553 Disappearance of the polar intensity minima and the transition to broad lobe structures

554 when averaged are taken over increasingly long times might simply be a consequence of a
555 lack of adequate spatial coverage in the geomagnetic and paleomagnetic data, especially at
556 high latitudes.

557 To illustrate this effect, Figure 11 shows time average radial magnetic fields on the outer
558 boundary from the Table A2 dynamo with $Ra = 6 \times 10^7$, $L2$ boundary heterogeneity and
559 neutral ($S=0$) stratification parameter. Panel a shows the field structure with truncation
560 at spherical harmonic degree and order $(\ell, m)_{max} = 24$; panel b is the same field with trun-
561 cation at $(\ell, m)_{max} = 12$, whereas panel c is the same field truncated at $(\ell, m)_{max} = 6$. This
562 figure illustrates the hazards of using limited-resolution geomagnetic field representations
563 to interpret high latitude structure on the CMB in terms of outer core stratification. The
564 fully-resolved field structure is squarely in the M (polar minima) regime, as are the weakly
565 filtered images in Figure 11a and b. However, the strongly filtered image Figure 11c removes
566 the polar minima, making the high latitude field appear more like the L (lobe) regime.

567 Similar trends emerge when the present-day geomagnetic field is subjected to increasingly
568 severe spherical harmonic truncation. Figure 12 shows the radial component of the geomag-
569 netic field on the CMB at epoch 2010 from the CHAOS field model (Olsen et al., 2014). Panel
570 a is the complete field model, with representation to spherical harmonic degree and order
571 $(\ell, m)_{max} = 14$. Intensity minima are evident at both poles at this resolution. Panels b and
572 c show the same field model truncated at spherical harmonic degree and order $(\ell, m)_{max} =$
573 12 and 6, respectively. The polar minima are strongly attenuated with increasingly severe
574 truncation, such that the southern polar minima is completely removed at $(\ell, m)_{max} = 6$ in
575 panel c, replaced by two broad, high intensity lobes. Since the data coverage necessarily
576 degrades in going from present-day to historical to archeomagnetic to paleomagnetic time
577 scales, a plausible interpretation of the trends shown in Figures 11 and 12 is that the longer
578 time span geomagnetic reconstructions lack the resolution necessary to resolve the true high
579 latitude field structure, would lead to an over-estimation of the stratification parameter S ,
580 and therefore would overestimate the amount of stratification presently below the CMB.

581 Because full resolution of the ancient core field is problematic, it is useful to consider
582 simpler diagnostics that would indicate stratification. Axially symmetric departures from an
583 axial dipole have been extensively investigated over the entire paleomagnetic record (Evans
584 1976; McFadden and Reid, 1982; Veikkolainen et al., 2014; Johnson and McFadden, 2015.)
585 The general consensus is that the ratio of axial quadrupole to axial dipole Gauss coefficients,

586 denoted by G_{20} , is nonzero at several epochs, whereas the ratio of axial octupole to axial
 587 dipole Gauss coefficients, denoted by G_{30} , is quite small when averaged over the past 0-5
 588 Ma, less than 0.05 in absolute value, with considerable debate concerning its sign. This is
 589 generally consistent with the more recent history of G_{30} , which is approximately -0.045 when
 590 averaged over the past decade and even smaller when averaged over the past ten millennia,
 591 -0.006 according to archeomagnetic field reconstruction CALS10k (Korte et al., 2011). When
 592 averaged over separate polarity chrons, paleomagnetic inclination data indicate $G_{30} \simeq 0.01$
 593 during the Brunhes chron, but somewhat larger $G_{30} \simeq 0.05$ during the Matuyama chron
 594 (Aubert et al., 2010). There is some evidence that G_{30} may have been far larger in the
 595 Precambrian (Evans and Hoyer, 2007; Veikkolainen et al., 2014) but back then the influence of
 596 inner core buoyancy release may have been less or non-existent. Indeed, numerical dynamos
 597 with a passive inner core (Heimpel and Evans, 2013) or no inner core at all (Landeau et al.,
 598 2017) generally produce larger and more positive values of G_{30} compared to similar dynamos
 599 with an active inner core.

600 The key question here is whether this evidence of a modest-sized G_{30} in the time-averaged
 601 field is large enough to validate stable stratification beneath the CMB. According to Figure
 602 8b, the observation that $G_{30} \leq 0.05$ when the geomagnetic field is averaged over the past
 603 few million years suggests a stratification parameter beneath the CMB of $S < 0.1$. According
 604 to (18), the size of G_{30} constrains the thickness of such a layer to 400 km or less, approxi-
 605 mately, and would seem to preclude very thick thermal stratification, such as the 1000 km
 606 layer proposed by Gomi et al. (2013), for which $S \simeq 0.2$ and $G_{30} \simeq 0.15$. However, this con-
 607 clusion is based on a limited set of dynamo calculations, and further exploration of partially
 608 stratified dynamos with different boundary conditions and control parameters is needed for
 609 confirmation.

610 Core flow inversions offer another way to probe for outer core stratification in localized
 611 regions beneath the CMB, including polar regions. Typically, flow core inversions based on
 612 the assumption of frozen magnetic flux find westward zonal flow in the polar regions (e.g.
 613 Eymin and Hulot, 2005; Amit and Olson, 2006), as in our low S cases, but unlike our higher
 614 S cases. By this measure, our neutral $S = 0$ or stratified $S = 0.1$ dynamos seem more Earth-
 615 like in terms of core flow, compared to the larger S dynamos. Is this strong enough evidence
 616 to say that the outermost core is at most weakly stratified? A recent inversion for core flow
 617 concluded that a purely horizontal (i.e., toroidal) flow fails to explain the global geomagnetic

618 SV (Lesur et al., 2015), but adding weak upwellings yields a better fit, a conclusion that is
619 basically consistent with weak stratification. Similarly, an even more localized frozen flux
620 study by Chulliat et al. (2010) confined to the north polar region argued for radial magnetic
621 diffusion supported by an underlying polar upwelling, i.e., at most weak stratification, in
622 basic agreement with Olson and Aurnou (1999).

623 We can also compare our results with inferences of outer core stratification derived from
624 idealized analytical models of thermochemical convection and from dynamical interpretations
625 of the geomagnetic secular variation. According to the convection model of Lister and Buffett
626 (1998), the present-day core is predicted to have $\delta \simeq 190$ km of thermal stratification for
627 the adiabatic and total heat fluxes listed in Table 1. For these same heat fluxes their model
628 predicts a maximum value of $(N/2\Omega)^2 \simeq 0.5$ at the cmb, compared to our maximum value of
629 1.1 calculated using (19). Buffett (2014) has proposed that a portion of the time-dependent
630 zonal flow in the outer core as well as the time-dependent deviations from uniform decrease
631 of the historical geomagnetic dipole moment are expressions of MAC oscillations – waves in
632 the outer core governed by magnetic, buoyancy (i.e., Archimedes) and Coriolis forces that
633 propagate in the north-south direction within a layer beneath the CMB, their propagation
634 characteristics depending on the stratification in the layer. The best-fitting model for MAC
635 wave propagation determined by Buffett et al. (2016) consists of an approximately 140 km
636 thick layer with peak stratification immediately below the CMB given by $(N/2\Omega)^2 \simeq 0.21$
637 and a layer average gravitational stability of $(N/2\Omega)^2 \simeq 0.1$, approximately. Their MAC
638 model stability is about 20% of our value and their stratified layer average value is about
639 13% of ours, based on (21). In terms of our scaling law (18) that relates the stratified layer
640 thickness to the stratification parameter, the Buffett et al. (2016) $\delta \simeq 140$ km corresponds
641 to $\delta^* \simeq 0.062$. Inverting (18) with $a=1.82$ and $b=1.2$ yields $S \simeq 0.042$. Referring to Figure
642 6, this value of the stratification parameter is expected produce a high latitude, time average
643 radial magnetic field structure of the M-type with polar minima, much like the present-day
644 geomagnetic field. For reference, such a stratified layer would have to increase to 600 km
645 or more in thickness in order to produce L-type lobes in the time average high latitude
646 geomagnetic field, according to our results. For the octupole field component, Figure 8
647 predicts a value of $G30 \simeq 0.08$ for $S=0.04$, somewhat higher than typically inferred from the
648 time-averaged paleomagnetic field over the past two polarity chrons, but probably within
649 the range of the combined dynamo model and observational uncertainties.

650 We conclude that a deep, thermally stratified layer beneath the CMB (nominally 1000 km
651 thick) would be detectable with our methods but is at variance with the observed structure of
652 the geomagnetic field. A thin thermally stratified layer beneath the CMB (a few hundred km
653 thick or less) is more consistent with observations but would be difficult to confirm using our
654 methods, because of uncertainties in long time average geomagnetic field reconstructions.
655 Detection of this amount of stratification may well be possible in the future, with better
656 resolution of the time-averaged geomagnetic field combined with more extensive modeling of
657 partially stratified dynamos.

658 **Acknowledgments**

659 This research was supported by Frontiers in Earth System Dynamics grant EAR-1135382
660 from the National Science Foundation. The dynamo calculations were made at the Maryland
661 Advanced Research Computer Center (MARCC). We benefited from insightful comments
662 and suggestions by Hagay Amit, and from thorough reviews by Phil Livermore and Bruce
663 Buffett.

664 **Author contributions**

665 PO and ML defined the numerical dynamo parameter sweep; ER did the dynamo calcu-
666 lations, collected and organized the numerical data; PO and ML did the scaling analysis,
667 interpretation, and wrote the paper.

References

- Amit, H., 2014. Can downwelling at the top of the Earth's core be detected in the geomagnetic secular variation? *Phys. Earth Planet. Inter.* 229, 110-121.
- Anzellini, S., Dewaele, A., Mezouar, M., Loubeyre, P., Morard, G., 2013. Melting of iron at Earth's inner core boundary based on fast X-ray diffraction. *Science* 340, 464-467.
- Aubert, J., Tarduno, J.A., Johnson, C.L., 2010. Observations and models of the long-term evolution of Earth's magnetic field. *Space Sci. Rev.* DOI 10.1007/s11214-010-9684-5.
- Braginsky, S. I., 1993. Mac-oscillations of the hidden ocean of the core. *J. Geomagn. Geoelectr.* 45, 1517-1538.
- Buffett, B., 2014. Geomagnetic fluctuations reveal stable stratification at the top of the Earth's core. *Nature* 507, 484-487.
- Buffett, B., Seagle, C., 2010. Stratification of the top of the core due to chemical interactions with the mantle. *J. Geophys. Res.* 115, B04407.
- Buffett, B., Knezek, N., Holme, R., 2016. Evidence for MAC waves at the top of Earth's core and implications for variations in length of day. *Geophys. J. Intern.* 204(3), 1789-1800.
- Christensen, U.R., Wicht, J., 2008. Models of magnetic field generation in partly stable planetary cores: Applications to Mercury and Saturn. *Icarus* 196, 16-34.
- Christensen, U.R., 2016. Geodynamo models with a thick stable layer and heterogeneous CMB heat flow. *sciencesconf.org:sedi2016:115015*, p 146.
- Chulliat, A., Hulot, G., Newitt, L.R., 2010. Magnetic flux expulsion from the core as a possible cause of the unusually large acceleration of the north magnetic pole during the 1990s. *J. Geophys. Res.* 115, B07101.
- Dziewonski, A. M., Anderson, D. L., 1981. Preliminary reference Earth model. *Phys. Earth Planet. Inter.* 25, 297-356.
- Dziewonski, A.M., Lekic, V., Romanowicz, B.A., 2010. Mantle anchor structure: an argument for bottom up tectonics. *Earth Planet. Sci. Lett.* 299, 69-79.

- 695 Evans, M.E., 1976. Test of the dipolar nature of the geomagnetic field throughout Phanero-
696 zoic time. *Nature* 262, 676-677.
- 697 Evans, M.E., Hoye, G.S., 2007. Testing the GAD throughout geological time. *Earth Planets*
698 *Space* 59 (7), 697-701.
- 699 Gomi, H., Ohta, K., Hirose, K., Labrosse, S., Caracas, R., Verstraete, M.J., Hernlund,
700 J.W., 2013. The high conductivity of iron and thermal evolution of the Earth's core.
701 *Phys. Earth Planet. Inter.* 224, 88-103.
- 702 Gubbins, D., 2007. Geomagnetic constraints on stratification at the top of Earth's core.
703 *Earth Planet. Space* 59, 661-664.
- 704 Gubbins, D., Davies, C., 2013. The stratified layer at the core-mantle boundary caused by
705 barodifusion of oxygen, sulfur and silicon. *Phys. Earth Planet. Int.* 215, 21-28.
- 706 Helffrich, G., Kaneshima, S., 2010. Outer-core compositional stratification from observed
707 core wave speed profiles. *Nature* 468, 807-810.
- 708 Helffrich, G., Kaneshima, S., 2013. Causes and consequences of outer core stratification.
709 *Phys. Earth Planet. Inter.* 223, 2-7.
- 710 Hirose, K., Labrosse, S., Hernlund, J., 2013. Composition and State of the Core. *Ann.*
711 *Rev. Earth Planet. Sci.* 41, 657-691.
- 712 Eymin, C., Hulot, G., 2005. On core surface flows inferred from satellite magnetic data.
713 *Phys. Earth Planet. Inter.* 152, 200-220.
- 714 Jackson A., Jonkers, A.R.T., Walker, M.R., 2000. Four centuries of geomagnetic secular
715 variation from historical records. *Phil. Trans. Roy. Soc. London, Series A* 358,
716 957-990.
- 717 Johnson, C., Constable, C.G., 1995. The time-averaged geomagnetic field as recorded by
718 lava flows over the last 5 Ma. *Geophys. J. Int.*, 122, 489-519.
- 719 Johnson, C.L., McFadden, P., 2015. The Time-Averaged Field and Paleosecular Varia-
720 tion. In: Gerald Schubert (editor-in-chief) *Treatise on Geophysics*, 2nd edition, Vol 5.
721 Oxford: Elsevier, 385-417.

- 722 Jones, C.A., 2007. Thermal and compositional convection in the core, In: *Treatise on*
723 *Geophysics*, vol. 8, ch 4, Olson, P., (ed.), Elsevier B.V., pp.131-186.
- 724 Jones, C.A., Boronski, P., Brun, A.S., Glatzmaier, G.A., Gastine, T., Miesch, M.S., Wicht,
725 J., 2011. Anelastic convection-driven dynamo benchmarks. *Icarus* 216(1), 120-135.
- 726 Kaneshima, S., 2017. Array analyses of SmKS waves and the stratification of Earth's
727 outermost core. *Phys. Earth Planet. Inter.* (in press).
- 728 Konopkova, Z., McWilliams, R. S., Gomez-Perez, N., Goncharov, A. F., 2016. Direct
729 measurement of thermal 583 conductivity in solid iron at planetary core conditions.
730 *Nature* 534 (7605), 99-101.
- 731 Korte, M., Constable, C., Donadini, F., Holme, R., 2011. Reconstructing the Holocene
732 Geomagnetic Field. *Earth Planet. Sci. Lett.* 312, 497-505.
- 733 Labrosse, S., 2015. Thermal evolution of the core with a high thermal conductivity. *Phys.*
734 *Earth Planet. Int.* 247, 36-55.
- 735 Landeau, M., Olson, P., Deguen, R., Hirsh, B., 2016. Core merging and stratification after
736 giant impacts. *Nature Geoscience* 9, 786-789.
- 737 Landeau, M., Aubert, J., Olson, P., 2017. The signature of inner-core nucleation on the
738 geodynamo. *Earth Planet Sci. Lett.* 465, 193-204, 2017.
- 739 Lay, T., Young, C., 1990. The stably-stratified outermost core revisited. *Geophys. Res.*
740 *Lett.* 17, 2001-2004.
- 741 Lesur, V., Whaler, K., Wardinski, I., 2015. Are geomagnetic data consistent with stably
742 stratified flow at the core-mantle boundary? *Geophys. J. Int.* 201, 929-946
- 743 Lister, J.R., Buffett, B.A., 1998. Stratification of the outer core at the core-mantle bound-
744 ary. *Phys. Earth Planet. Inter.* 105, 5-19.
- 745 Masters, G., Gubbins, D., 2003. On the resolution of density within the Earth. *Phys.*
746 *Earth Planet. Inter.* 140, 159-167.
- 747 Nakagawa, T., 2011. Effect of a stably stratified layer near the outer boundary in numerical
748 simulations of a magnetohydrodynamic dynamo in a rotating spherical shell and its
749 implications for Earth's core. *Phys. Earth Planet. Inter.* 187, 342-352.

750 Nakagawa, T., Tackley, P. J., 2013. Implications of high core thermal conductivity on
751 Earth's coupled mantle and core evolution. *Geophys. Res. Lett.* 40(11), 2652-2656.

752 Nakagawa, T., Tackley, P. J., 2015. Influence of combined primordial layering and recycled MORB on the coupled thermal evolution of Earth's mantle and core. *Geochem., Geophys., Geosyst.* 15(3), 619-633.

755 Nakagawa, T., 2015. An implication for the origin of stratification below the core-mantle
756 boundary region in numerical dynamo simulations in a rotating spherical shell. *Phys. Earth Planet. Inter.* 247, 94-104.

758 Nakagawa, T., 2017. On the thermo-chemical origin of the stratified region at the top of
759 the Earth's core. *Phys. Earth Planet. Inter.* (in press).

760 Ohta, K., Kuwayama, Y., Hirose, K., Shimizu, K., Ohishi, Y., 2016. Experimental determination of the electrical resistivity of iron at earth's core conditions. *Nature* 534 (7605),
761 95-98.

763 Olsen, N., Luhr, H., Finlay, C., Sabaka, T., Michaelis, I., Rauberg, J., Tner-Clausen, L.,
764 2014. The chaos-4 geomagnetic field model. *Geophys. J. Int.* 197 (2), 815-827.

765 Olson, P., Aurnou, J., 1999. A polar vortex in the Earth's core. *Nature* 402, 170-173.

766 Olson, P., Amit, H., 2015. Mantle superplumes induce geomagnetic superchrons. *Frontiers in Earth Science* 3 (38) doi: 10.3389/feart.2015.00038.

768 Olson, P., Amit, H., 2006. Changes in Earth's dipole. *Naturwissenschaften* 93, 519-542.

769 Olson, P., Deguen, R., Rudolph, M.L., Zhong, S., 2015. Core evolution driven by mantle
770 global circulation. *Phys. Earth Planet. Inter.* 243, 44-55.

771 Perrillat, J.-P., Mezouar, M., Garbarino, G., Bauchau, S., 2010. In situ viscometry of high-
772 pressure melts in the Paris-Edinburgh cell: application to liquid FeS. *High Pressure Research* 30 (3), 415-423.

774 Poirier, J.-P., 2000. Introduction to the physics of the Earth's interior, 2nd Edition. Cambridge University Press.

775

- 776 Rudolph, M., Zhong, S.J., 2014. History and dynamics of net rotation of the mantle and
777 lithosphere. *Geochem. Geophys. Geosyst.*, 10.1002/2014GC005457.
- 778 Sreenivasan, B., Jones, C. A., 2005. Structure and dynamics of the polar vortex in the
779 earth's core. *Geophys. Res. Lett.* 32 (20), doi: 10.1029/2005GL023841.
- 780 Takehiro, S.-I., Sasaki, Y., 2017. Penetration of steady fluid motions into an outer stable
781 layer excited by MHD thermal convection in rotating spherical shells. *Phys. Earth
782 Planet. Inter.* <http://dx.doi.org/10.1016/j.pepi.2017.03.001>.
- 783 Tanaka, S., 2007. Possibility of a low p-wave velocity layer in the outermost core from
784 global smks waveforms. *Earth Planet. Sci. Lett.* 259, 486-499.
- 785 Tang, V., Zhao, L., Hung, S., 2015. Seismological evidence for a non-monotonic velocity
786 gradient in the topmost outer core. *Sci. Rep.* 5, 8613.
- 787 Turner, J.S., 1980. *Buoyancy effects in fluids*, Cambridge University Press ISBN 9780521297264.
- 788 Veikkolainen, T., Pesonen, L.J., Korhonen, K., Evans, D.A.D., 2014. On the low-inclination
789 bias of the Precambrian geomagnetic field. *Precambrian Research* 244, 23-32.
- 790 Vocadlo, L., Alfe, D., Gillan, M. J., Price, G. D., 2003. The properties of iron under core
791 conditions from first principles calculations. *Phys. Earth Planet. Inter.* 140, 101-125.
- 792 Yadav, R.K., Gastine, T., Christensen, U.R., Duarte, L.D., 2013. Consistent scaling laws
793 in anelastic spherical shell dynamos. *Astrophys. J.* 774(1), 6.
- 794 Whaler, K., 1980. Does the whole of the Earth's core convect? *Nature* 287, 528-5530.
- 795 Wicht, J., 2002. Inner-core conductivity in numerical dynamo simulations. *Phys. Earth
796 Planet. Inter.* 132, 281-302.
- 797 Zhong, S.J., Rudolph, M.L., 2015. On the temporal evolution of long-wavelength man-
798 tle structure of the Earth's mantle since the Early Paleozoic. *Geochem. Geophys.
799 Geosyst.* 16, 1599-1615.

800 Appendix

801 Governing equations

802 Using the notation from Section 2, we define the codensity in the outer core as the sum
 803 of a spatially uniform background state ($C_o + C_{icb}$) with a time-dependent part denoted by
 804 subscript o , plus a deviation from that state C , defined so that

$$C_o + C = \rho_o(\alpha(T_o + T) + \beta(\chi_o + \chi)), \quad (22)$$

805 where T and χ are the outer core variations in temperature and light element concentration,
 806 respectively. We take the background temperature to be adiabatic, with its mean value
 807 denoted by $T_o = T_{ad}$. The rate-of-change of the background codensity (assumed constant in
 808 each calculation) is then

$$\dot{C}_o = \rho_o(\alpha\dot{T}_{ad} + \beta\dot{\chi}_o). \quad (23)$$

809 Scaling length, time, codensity, and magnetic field with D , D^2/ν , $D^2\rho\beta\dot{\chi}_o/\nu$ and $\sqrt{\rho_o\Omega/\sigma}$
 810 as in Section 2, the dimensionless Boussinesq equations of motion are

$$E\left(\frac{d\mathbf{u}^*}{dt^*} - \nabla^2\mathbf{u}^*\right) + 2\hat{z} \times \mathbf{u}^* + \nabla P^* = EPr^{-1}Ra\left(\frac{\mathbf{r}}{r_{cmb}}\right)C^* + Pm^{-1}(\nabla \times \mathbf{B}^* \times \mathbf{B}^*), \quad (24)$$

811

$$\frac{\partial \mathbf{B}^*}{\partial t^*} = \nabla \times (\mathbf{u}^* \times \mathbf{B}^*) + Pm^{-1}\nabla^2\mathbf{B}^*, \quad (25)$$

812 and

$$\frac{dC^*}{dt^*} = Pr^{-1}\nabla^2C^* + \epsilon, \quad (26)$$

813 where

$$\epsilon = \frac{Ra_{ad}}{Ra} - 1 \quad (27)$$

814 in which

$$Ra = \frac{\beta g D^5 \dot{\chi}_o}{\nu^2 \kappa}, \quad (28)$$

815 as in Section 2, and

$$Ra_{ad} = -\frac{\alpha g D^5 \dot{T}_{ad}}{\nu^2 \kappa} \quad (29)$$

816 is the Rayleigh number measuring the cooling of the core. The other dimensionless control
 817 parameters are

$$E = \frac{\nu}{\Omega D^2}; \quad Pr = \frac{\nu}{\kappa}; \quad Pm = \frac{\nu}{\eta}. \quad (30)$$

Table A1: CMB Heat Flow Heterogeneity Coefficients

Type	ℓ	m	real ^a	imag ^a
L2	2	0	-0.0479	0.0000
L2	2	2	0.0526	-0.0447
L4	1	0	-0.0163	0.0000
L4	1	1	0.0232	-0.0248
L4	2	0	-0.0479	0.0000
L4	2	1	0.0054	-0.0258
L4	2	2	0.0526	-0.0447
L4	3	0	0.0253	0.0000
L4	3	1	-0.0059	0.0016
L4	3	2	0.0203	0.0107
L4	3	3	-0.0075	0.0333
L4	4	0	-0.0150	0.0000
L4	4	1	-0.0011	-0.0028
L4	4	2	-0.0035	-0.0006
L4	4	3	-0.0171	-0.0126
L4	4	4	0.0138	0.0092

^a Amplitude coefficients of fully normalized, complex spherical harmonics

Table A2: Dynamo Cases

Ra	S	L	CMB C^*	Min. C^*	δ^*	N^{*2}	Structure
1.0×10^7	0.1	4	0.704284	0.697211	0.1104	0.0640	M/P
1.0×10^7	0.1	2	0.693749	0.68662	0.1033	0.0690	M
1.0×10^7	-0.1	2	0.517744	0.517744	0	NA	M
1.0×10^7	-0.1	4	0.521391	0.521391	0	NA	M
1.0×10^7	0	2	0.600992	0.600992	0	NA	M
1.0×10^7	0	4	0.604899	0.604899	0	NA	M
2.0×10^7	0.1	2	0.764032	0.757908	0.0922	0.0663	M
2.0×10^7	0.2	2	0.862358	0.832471	0.2209	0.1352	P
2.0×10^7	0.2	0	0.859579	0.822195	0.2417	0.1546	-
2.0×10^7	0.3	2	0.978527	0.893147	0.3755	0.2273	L
2.0×10^7	0.4	2	1.23117	1	0.6491	0.3561	N
2.0×10^7	0.5	2	1.51669	1	0.6491	0.7960	N
2.0×10^7	1	4	2.93827	1	0.6491	2.986	N
2.0×10^7	-0.1	2	0.643534	0.643534	0	NA	M
2.0×10^7	-0.1	0	0.643641	0.643641	0	NA	M
2.0×10^7	0	2	0.692374	0.692374	0	NA	M
3.0×10^7	0.1	2	0.803259	0.794543	0.1241	0.0702	M
3.0×10^7	0.2	2	0.882598	0.853013	0.2092	0.1414	P
3.0×10^7	0.3	2	0.985372	0.898129	0.3853	0.2264	L
3.0×10^7	0.3	0	1.01468	0.920806	0.3963	0.2368	-
3.0×10^7	0.4	2	1.23201	1	0.6491	0.3574	N
3.0×10^7	0.5	2	1.51755	1	0.6491	0.7973	N
3.0×10^7	0	2	0.744316	0.744316	0	NA	M
4.0×10^7	0.1	2	0.824921	0.815779	0.1254	0.0729	M
4.0×10^7	0.2	2	0.896273	0.864884	0.2326	0.1349	P
4.0×10^7	0.3	2	0.999349	0.913303	0.3866	0.2225	L
4.0×10^7	0.4	2	1.23271	1	0.6491	0.3585	N
4.0×10^7	0.5	2	1.51825	1	0.6491	0.7984	N
4.0×10^7	-0.1	2	0.73243	0.73243	0	NA	M
4.0×10^7	0	2	0.775396	0.775396	0	NA	M
5.0×10^7	0.1	2	0.840957	0.830989	0.1487	0.0669	M
5.0×10^7	0.2	2	0.9071	0.8764	0.2371	0.1294	P
5.0×10^7	0.3	2	1.00609	0.919471	0.3892	0.2225	L
5.0×10^7	0.4	2	1.23331	1	0.6491	0.3594	N
5.0×10^7	0.5	2	1.51883	1	0.6491	0.7993	N

Table A2: Continued

Ra	S	L	CMB C^*	Min. C^*	δ^*	N^{*2}	Structure
6.0×10^7	0	2	0.812963	0.812782	0.0571	0.0032	M
6.0×10^7	0	0	0.815215	0.81507	0.0331	0.0044	M
6.0×10^7	0.1	2	0.852811	0.844548	0.1273	0.0648	M
6.0×10^7	0.1	0	0.856437	0.846691	0.1383	0.0704	M
6.0×10^7	0.2	2	0.913068	0.882692	0.2495	0.1217	P
6.0×10^7	0.2	0	0.919266	0.884893	0.2657	0.1293	-
6.0×10^7	0.3	2	1.01299	0.9276	0.3788	0.2254	L
6.0×10^7	0.3	0	1.02607	0.93166	0.4041	0.2336	-
6.0×10^7	0.4	2	1.23071	1	0.6491	0.3554	N
6.0×10^7	0.4	0	1.24977	1	0.6491	0.3848	N
6.0×10^7	0.5	2	1.51621	1	0.6491	0.7953	N
6.0×10^7	0.5	0	1.53475	1	0.6491	0.8238	N
6.0×10^7	-0.1	2	0.777253	0.777253	0	NA	M
6.0×10^7	-0.1	0	0.77527	0.77527	0	NA	M
7.0×10^7	0	2	0.822773	0.822546	0.0506	0.0045	M
7.0×10^7	0.1	2	0.865818	0.854998	0.1455	0.0743	M
7.0×10^7	0.2	2	0.922185	0.889587	0.2741	0.1189	P/M
7.0×10^7	0.3	2	1.0149	0.929291	0.3905	0.2192	L
8.0×10^7	0.1	2	0.873372	0.862076	0.1624	0.0695	M
8.0×10^7	0.2	2	0.927032	0.89635	0.2534	0.1211	M
8.0×10^7	0.3	2	1.01797	0.932767	0.3820	0.2230	L
9.0×10^7	0	2	0.84325	0.842954	0.0760	0.0039	M
9.0×10^7	0.1	2	0.877763	0.868198	0.1539	0.0621	M
9.0×10^7	0.2	2	0.929826	0.897254	0.2534	0.1285	M
9.0×10^7	0.3	2	1.01873	0.933266	0.3801	0.2248	L
1.0×10^8	0.05	2	0.865793	0.861533	0.1117	0.0381	M
1.0×10^8	0.1	2	0.886055	0.874903	0.1754	0.0636	M
1.0×10^8	0.15	2	0.90753	0.888956	0.1903	0.0976	M
2.0×10^8 ^a	0.1	0	0.85105	0.84252	0.120	0.0710	M
2.0×10^8 ^a	0.1	2	0.85196	0.84456	0.114	0.0649	M
2.0×10^8 ^a	0.1	4	0.85411	0.84590	0.127	0.0646	M

^a Cases with $E = 3 \times 10^{-5}$; all others with $E = 1 \times 10^{-4}$.

Table A3: Core Properties

Input Properties	Notation	Value
ICB radius	r_{icb}	1220 km ^a
CMB radius	r_{cmb}	3480 km ^a
Density at core center	ρ_c	12500 kg.m ⁻³ ^a
Density at zero pressure	ρ_0	7500 kg.m ⁻³
Mean core density	ρ_o	11040 kg.m ⁻³ ^a
Gravity at the CMB	g	10.68 m.s ⁻² ^a
Compositional density jump at the ICB	$\Delta\rho$	500 kg.m ⁻³ ^b
Incompressibility at zero pressure	K_0	4.75×10^{11} Pa
Melting temperature at the ICB	T_{melt}	5800 K ^c
Entropy of melting	ΔS	120 J.kg ⁻¹ .K ⁻¹ ^d
Grüneisen parameter	γ	1.5 ^e
Specific heat	C_p	850 J.kg ⁻¹ .K ⁻¹ ^e
Thermal expansion coefficient	α	1.3×10^{-5} K ⁻¹ ^e
Compositional expansion coefficient	β	1
Thermal conductivity	k	100 W.m ⁻¹ .K ⁻¹
Density length scale	r_ρ	6600 km ^a
Temperature length scale	r_T	6040 km ^c
Outer core light elements	χ	9.8 wt.% ^f
Mass of the core	M_c	1.95×10^{24} kg
Outer core kinematic viscosity	ν	$(2,7,22) \times 10^{-6}$ m ² .s ⁻¹ ^g
Outer core diffusivity	κ	10ν
Mean CMB heat flux	\bar{q}_{total}	79 mW.m ⁻²
Adiabatic CMB heat flux	q_{ad}	96 mW.m ⁻²
Output Parameters	Notation	Value
Light element concentration change rate	$\dot{\chi}_o$	3.2×10^{-16} s ⁻¹
Cooling rate	\dot{T}_o	-3.7×10^{-15} K.s ⁻¹
Codensity change rate	\dot{C}_o	6.8×10^{-16} kg s ⁻¹
Codensity sink	ϵ	-0.8
Rayleigh number	Ra	$(9 \times 10^{29}, 2 \times 10^{28}, 6 \times 10^{26})$
Stratification parameter	S	(0.018, 0.064, 0.2)
Stratified layer thickness	δ	(52, 230, 920) km
Stratified layer stability (CMB, ave.)	N^2	$(2.4, 1.7) \times 10^{-8}$ rad ² .s ⁻²

^a Dziewonski and Anderson (1981); ^b Masters and Gubbins (2003); ^c Ancellini et al. (2013);^d Poirier (1990); ^e Vocado et al. (2003); ^f Hirose et al. (2013); ^g Perriallt et al. (2010).

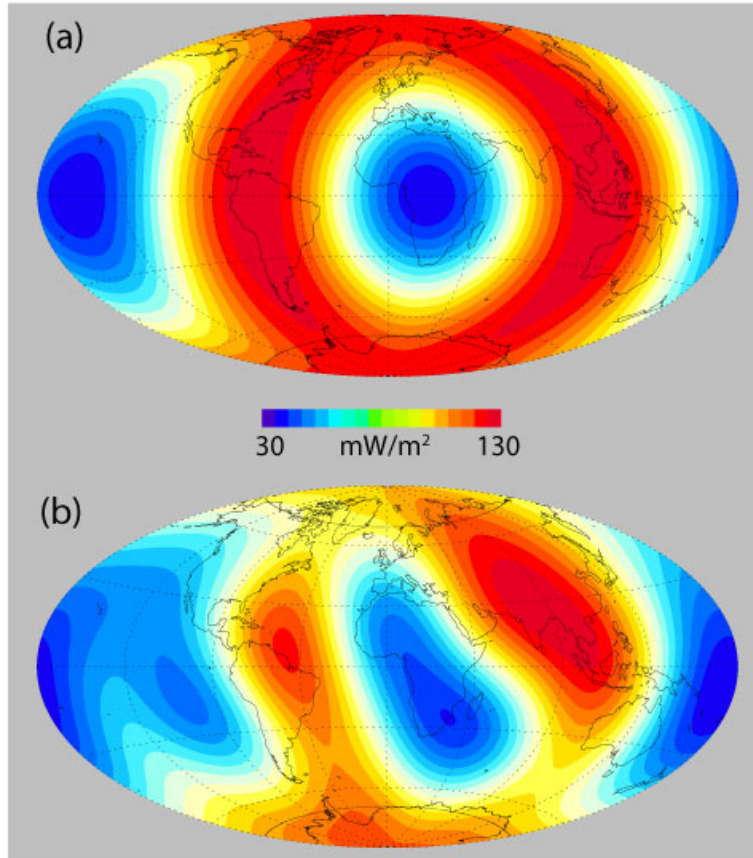


Figure 1: Core-mantle boundary heat flux patterns $L2$ (a) and $L4$ (b) used in this study.

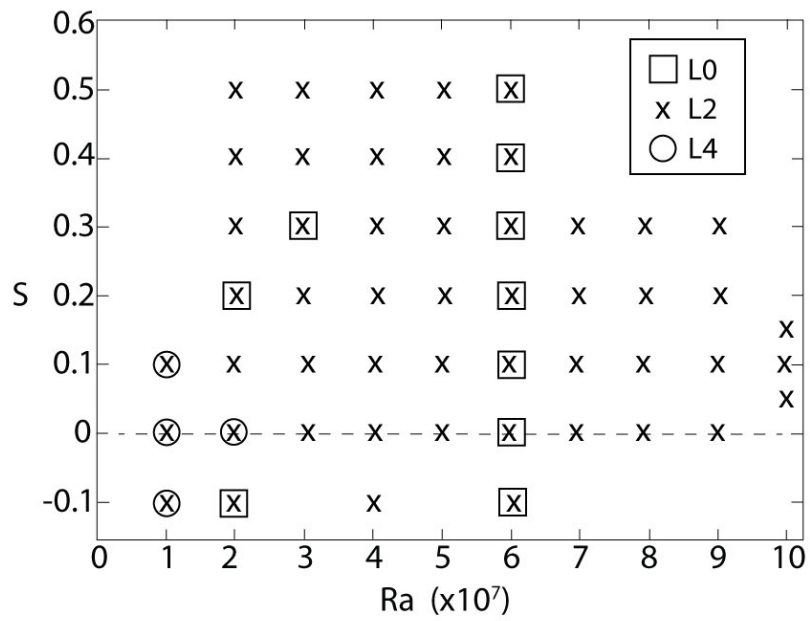


Figure 2: Regime diagram showing numerical dynamos used in this study as a function of the primary control parameters Ra and S . Insert shows symbols that refer to the type of outer boundary heterogeneity.

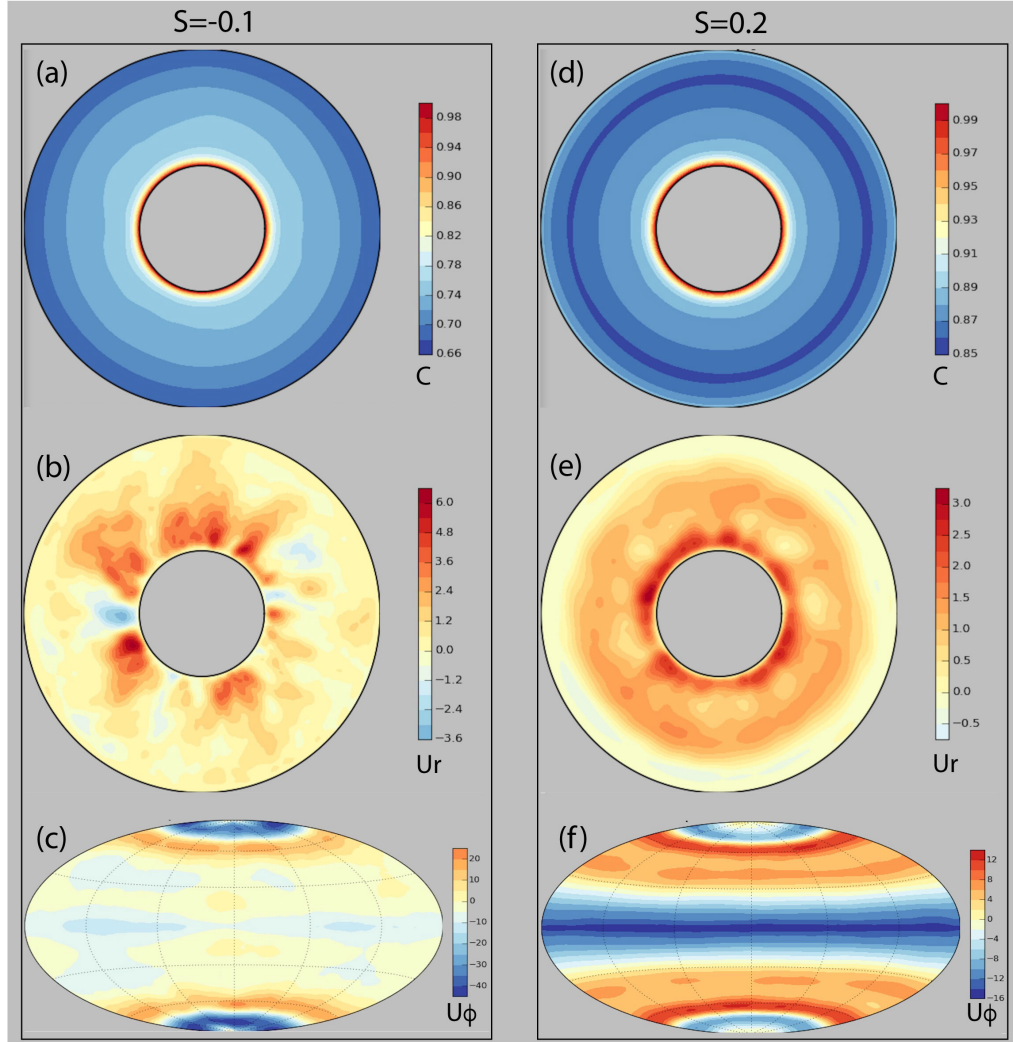


Figure 3: Equatorial plane and global Aitoff projection views of the time average flow structure at $E = 1 \times 10^{-4}$ and $Ra = 2 \times 10^7$ with $L0$ boundary heterogeneity, for boundary stratification parameters $S=-0.1$ (left column) and $S=0.2$ (right column). From top to bottom images show equatorial plane codensity (a,d), radial velocity (b,e) and azimuthal velocity at $0.95r_{cmb}$ (c,f). Velocity scales are in dimensionless Reynolds number uD/η units, u being the appropriate dimensional velocity component. Longitude increases anti-clockwise starting from the right edge (3 pm) in each equatorial image and to the right of the centerline in the global projections.

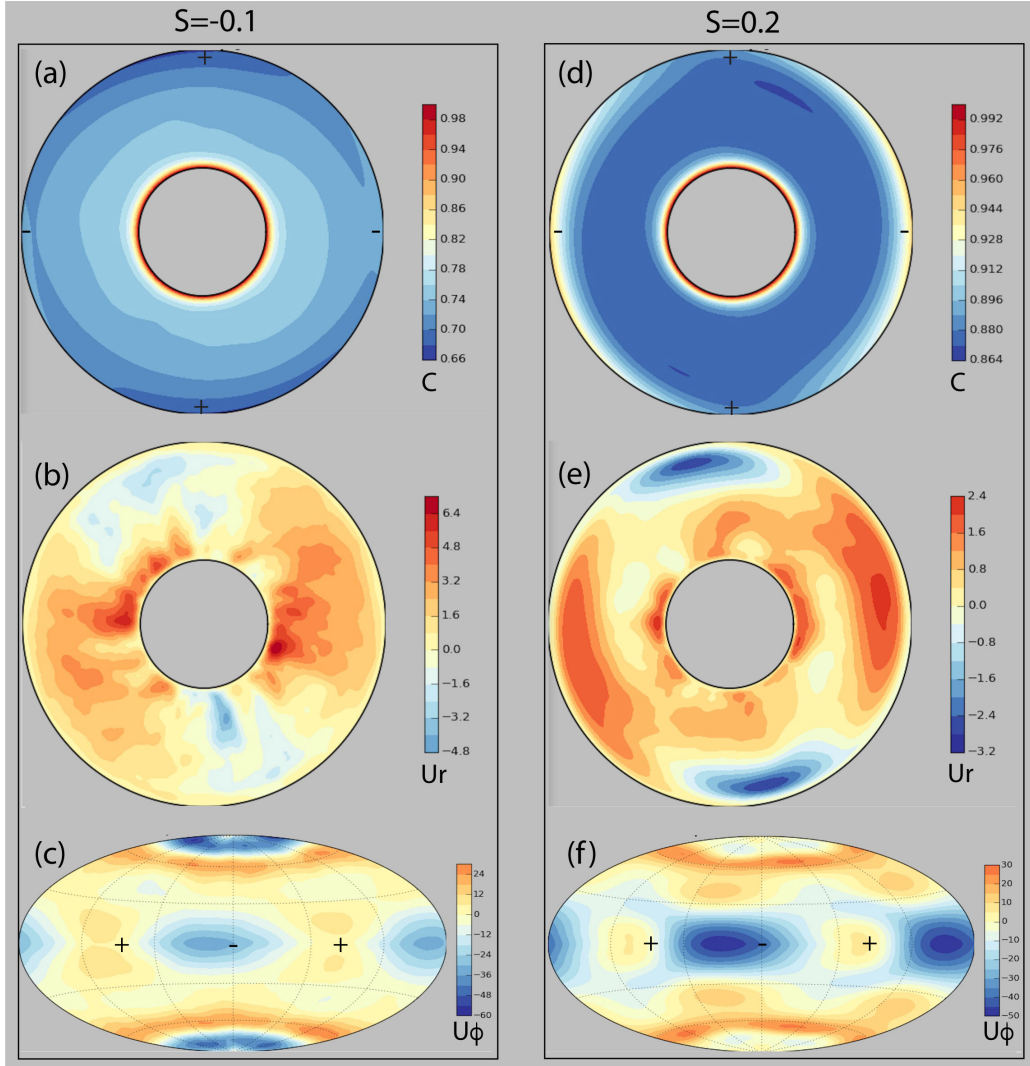


Figure 4: Equatorial plane and global Aitoff projections of the time average flow structure at $E = 1 \times 10^{-4}$ and $Ra = 2 \times 10^7$ with $L2$ boundary heterogeneity, for boundary stratification parameters $S=-0.1$ (left column) and $S=0.2$ (right column). From top to bottom images show equatorial plane codensity (a,d), radial velocity (b,e) and azimuthal velocity at $0.95r_{cmb}$ (c,f). Velocity scales are in Reynolds number units, as in Figure 3. Longitude increases anti-clockwise starting from the right edge (3 pm) in each equatorial image and to the right of the centerline in the global projections. Plus (+) and minus (-) signs indicate the longitudes of maximum and minimum boundary heat flux, respectively.

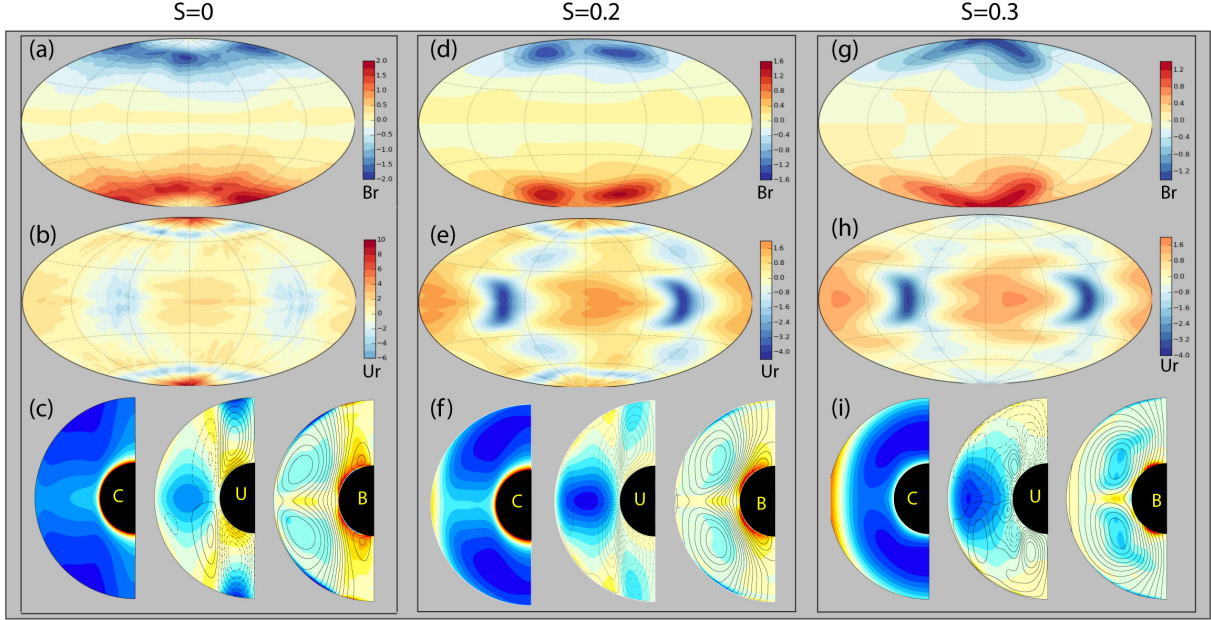


Figure 5: Global Aitoff projections and zonal averages of the time average dynamo structure at $E = 1 \times 10^{-4}$ and $Ra = 6 \times 10^7$ with $L2$ boundary heterogeneity, for boundary stratification parameters $S=0$ (left column), $S=0.2$ (middle column) and $S=0.3$ (right column). Top row images (a,d,g) show radial magnetic field at r_{cmb} . Middle row images (b,e,h) show radial velocity at $0.95r_{cmb}$. Bottom row images (c, f, i) show zonal averages of codensity (C), meridional streamlines over azimuthal velocity contours (U), and poloidal magnetic field lines over azimuthal field contours, with (blue,red) and (dashed, solid) contours indicating (negative, positive) values, respectively. Magnetic field scale bars are in dimensionless Elsasser number $\sqrt{\sigma/\rho_o}\Omega B_r$ units, where σ is electrical conductivity; likewise the velocity scale bars are in dimensionless Reynolds number uD/η units, u being the appropriate dimensional velocity component. Longitude increases to the right of the centerline in the global projections.

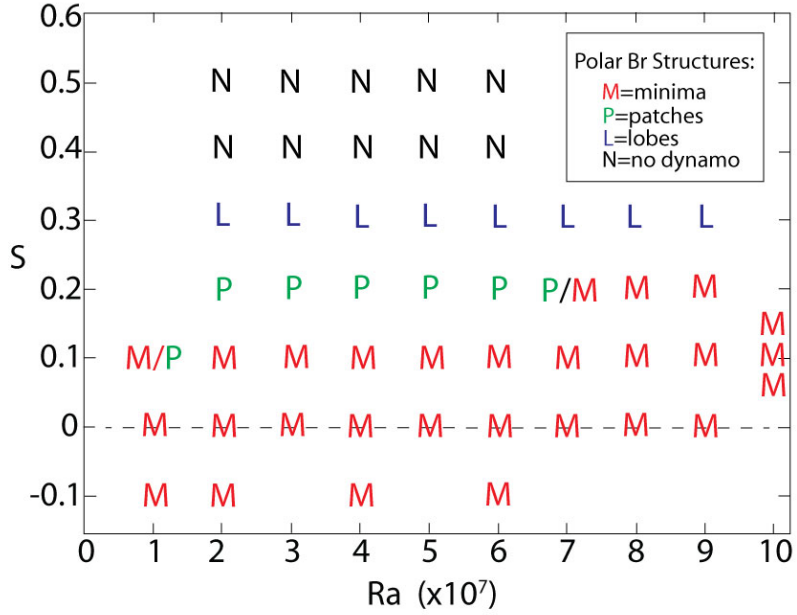


Figure 6: Regime diagram showing $E = 1 \times 10^{-4}$, $L2$ dynamo results for the time average radial magnetic field structure on the outer (core-mantle) boundary at high latitudes.

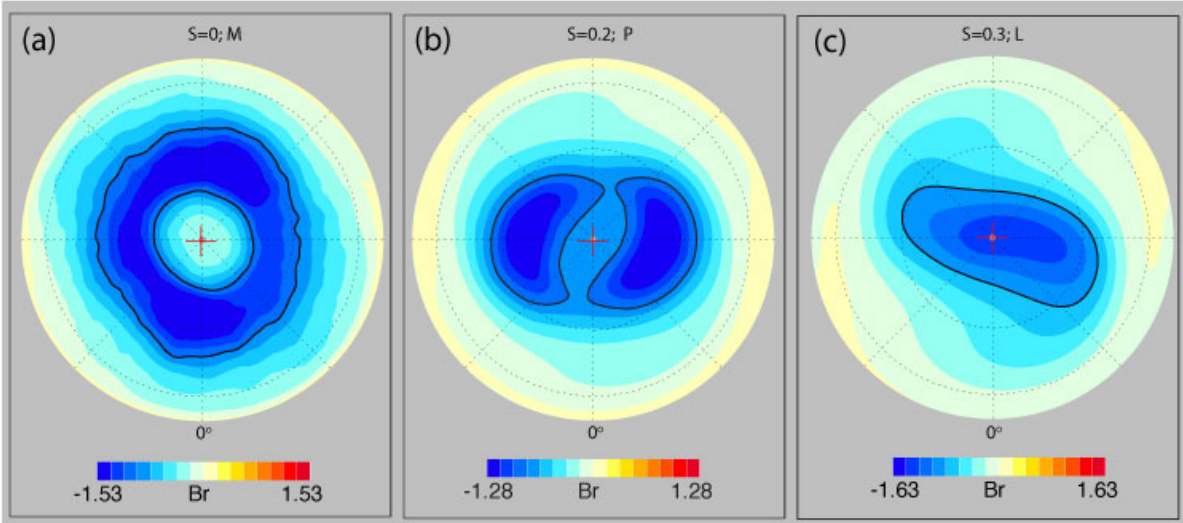


Figure 7: Polar views of time-averaged radial magnetic fields on the outer boundary from the dynamo in Figure 5. Solid black lines indicate bounding contours used for labeling field structures. a: Polar minimum M-structure with $S=0$ stratification parameter; b: Patch P-structure with $S=0.2$; c: Lobe L-structure with $S=0.3$. Magnetic intensity scale bars are in dimensionless Elsasser number units; red crosses mark the time-averaged geomagnetic pole.

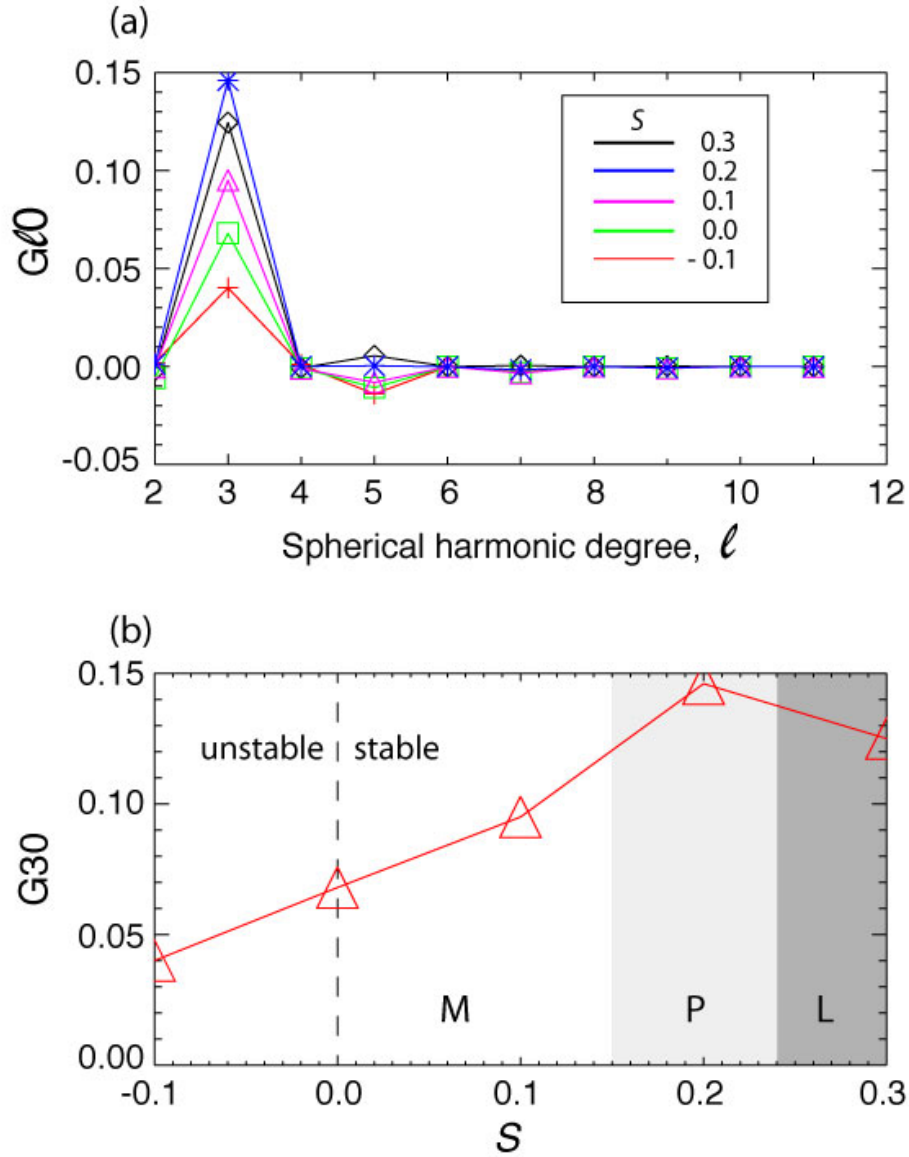


Figure 8: a: Axially symmetric ($m=0$) Gauss coefficient ratios versus spherical harmonic degree from time averaged dynamos with $Ra = 6 \times 10^7$ and $L2$ boundary heterogeneity, for various stratifications. b: Gauss coefficient ratio $G30$ versus stratification parameter S for the same dynamos. M,P,L denote polar minima, patches, and lobes, respectively, in the high latitude magnetic field structure. Stable/unstable refers to the stratification below the outer boundary.

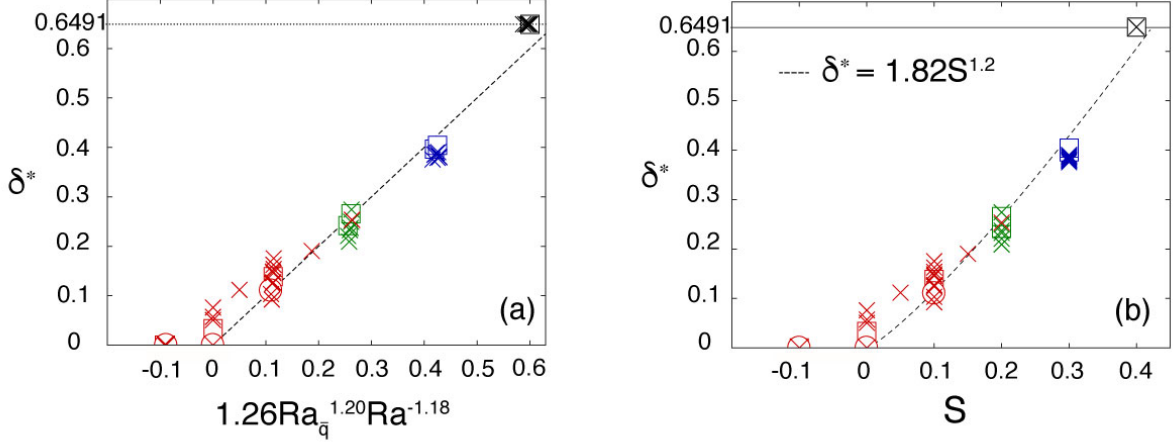


Figure 9: a: Dimensionless thickness of the stratified layer as a function of its best fit in terms of $Ra_{\bar{q}}$ and Ra as defined in the main text. The layer thickness is normalized by the core radius such that its maximum value is 0.6491. b: Dimensionless thickness of the stratified layer as a function of $S = Ra_{\bar{q}}/Ra$ alone. Dotted lines shows the least square best fits. Circles, squares and crosses denote $L0$, $L4$ and $L2$ boundary conditions, respectively. The symbol color varies progressively with Ra from light grey for $Ra = 10^7$ to black for $Ra = 10^8$. Simulations with $S > 0.4$ have been excluded for these fits since the stratified layer reaches its maximal value near $S = 0.4$ (where it invades the whole outer core).

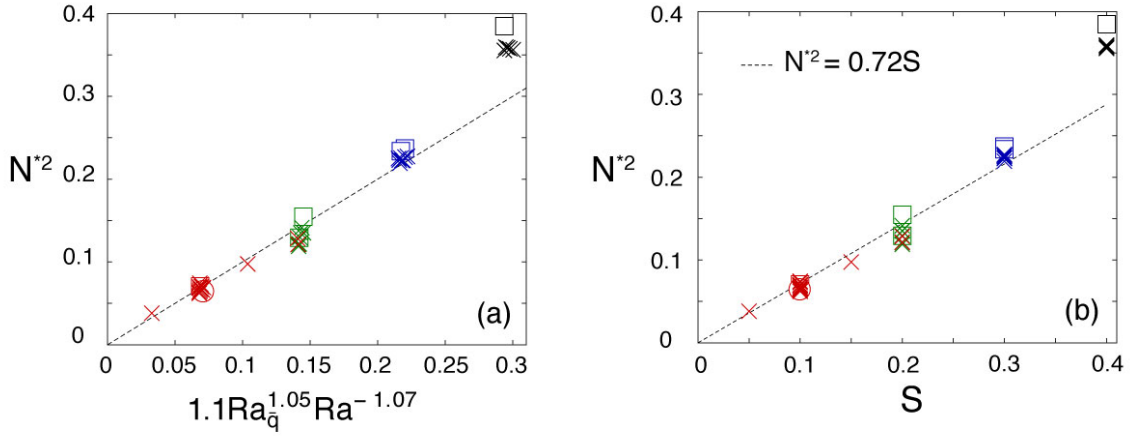


Figure 10: a: Dimensionless stability parameter as a function of its best fit in terms of $Ra_{\bar{q}}$ and Ra as defined in the main text. b: Same parameter as a function of $S = Ra_{\bar{q}}/Ra$ alone. Dotted lines shows the least square best fits. Circles, squares and crosses denote $L0$, $L4$ and $L2$ boundary conditions, respectively. Colors denote the different regimes for the time-averaged magnetic field structures: red for minima (regime M), green for patches (regime P), blue for lobes (regime L) and black for no dynamo (N). The symbol color varies progressively with Ra from light grey for $Ra = 10^7$ to black for $Ra = 10^8$. Simulations with $S \geq 0.4$, in which the layer invades the whole outer core have been excluded from the fits.

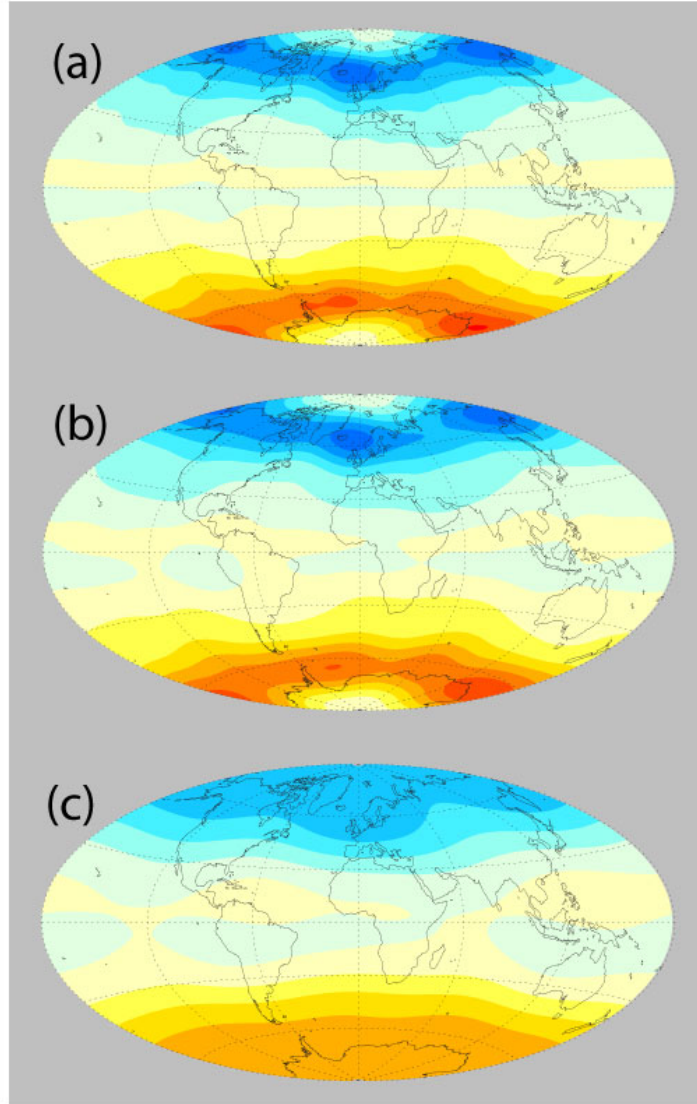


Figure 11: Time average radial magnetic fields on the outer boundary from the dynamo case with $Ra = 6 \times 10^7$ and $L2$ boundary heterogeneity and neutral ($S=0$) stratification parameter. a: truncation at spherical harmonic degree and order $(\ell, m)_{max} = 24$; b: truncation at $(\ell, m)_{max} = 12$; c: truncation at $(\ell, m)_{max} = 6$.

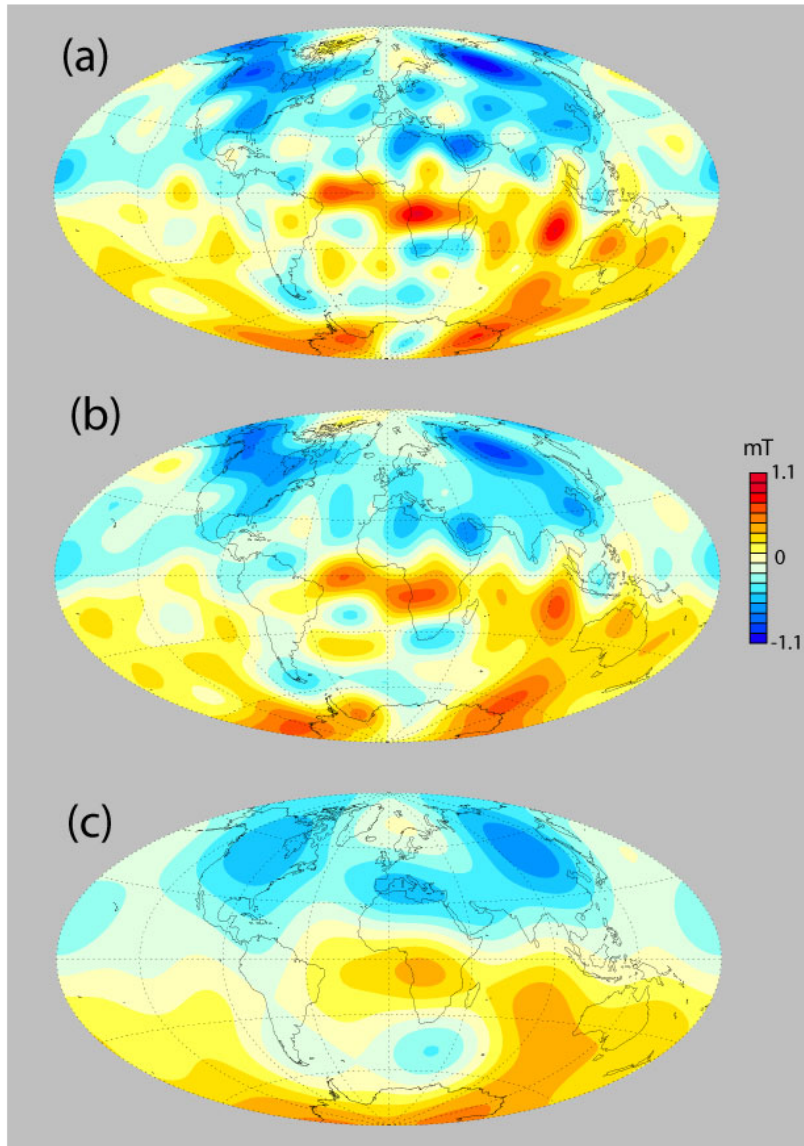


Figure 12: Radial magnetic fields on the CMB from the CHAOS4 2010 geomagnetic field model (Olsen et al., 2014) a: truncation at spherical harmonic degree and order $(\ell, m)_{max}=14$; b: truncation at $(\ell, m)_{max}=12$; c: truncation at $(\ell, m)_{max}=6$.